Dynamics of Strombolian explosions: Inferences from field and laboratory studies of erupted bombs from Stromboli volcano

Lucia Gurioli, L. Colo, A.J. Bollasina, Andrew J.L. J.L. Harris, Alan Whittington, M. Ripepe

AGU PUBLICATIONS

JGR

Journal of Geophysical Research: Solid Earth

RESEARCH ARTICLE
10.1002/2013JB010355

Key Points:
- Quantify variations in the degassing history of shallow basaltic magma
- Quantify the rheology of basaltic magma in the shallow system at Stromboli
- Redefine a model for strombolian explosions

Supporting Information:
- Readme
- Table S1
- Table S2
- Figure S2

Correspondence to:
L. Gurioli,
L.Gurioli@opgc.univ-bpclermont.fr

Citation:
Gurioli, L., L. Colo', A. J. Bollasina, A. J. L. Harris, A. Whittington, and M. Ripepe (2014), Dynamics of Strombolian explosions: Inferences from field and laboratory studies of erupted bombs from Stromboli volcano, *J. Geophys. Res. Solid Earth*, *119*, 319–345, doi:10.1002/2013JB010355.

Received 15 MAY 2013
Accepted 23 DEC 2013
Accepted article online 28 DEC 2013
Published online 29 JAN 2014

Dynamics of Strombolian explosions: Inferences from field and laboratory studies of erupted bombs from Stromboli volcano

L. Gurioli[1,2,3], L. Colo'[4], A. J. Bollasina[5], A. J. L. Harris[1,2,3], A. Whittington[5], and M. Ripepe[4]

[1]Laboratoire Magmas et Volcans, BP 10448, Clermont Université, Université Blaise Pascal, Clermont-Ferrand, France, [2]CNRS, UMR 6524, LMV, Clermont-Ferrand, France, [3]IRD, R 163, LMV, Clermont-Ferrand, France, [4]Dipartimento di Scienze della Terra, Università degli Studi di Firenze, Florence, Italy, [5]Department of Geological Sciences, University of Missouri, Columbia, Missouri, USA

Abstract Strombolian activity is characterized by repeated, low energy, explosions and is named after the volcano where such activity has persisted for around 2000 years, i.e., Stromboli (Aeolian Islands, Italy). Stromboli represents an excellent laboratory where measurements of such explosions can be made from safe, but close, distances. During a field campaign in 2008, two 15 cm diameter bombs were quenched and collected shortly after a normal explosion. The bombs were characterized in terms of their textural, chemical, rheological, and geophysical signatures. The vesicle and crystal size distribution of the samples, coupled with the glass chemistry, enabled us to quantify variations in the degassing history and rheology of the magma resident in the shallow (i.e., in last 250 m of conduit length). The different textural facies observed in these bombs showed that fresh magma was mingled with batches of partially to completely degassed, oxidized, high-crystallinity, high-viscosity, evolved magma. This magma sat at the top of the conduit and played only a passive role in the explosive process. The fresh, microlite-poor, vesiculated batch, however, experienced a response to the explosive event, by undergoing rapid decompression. Integration of geophysical measurements with sample analyses indicates that popular bubble-bursting models may not fit this case. We suggest that the degassed, magma forms a plug, or rheological layer, at the top of the conduit, through which the fresh magma bursts. In this model we need to consider the paradox of a slug ascending too fast through a magma of varying viscosity and yield strength.

1. Introduction

Slow magma ascent and/or ascent of bubbles in a low viscosity magma to generate foam have long been associated with low-intensity Strombolian activity [e.g., *Wilson and Head*, 1981; *Jaupart and Vergniolle*, 1988]. Transitions between effusive and explosive activity (fountaining, Strombolian, and more energetic eruptive styles) have been explained in terms of changes in the magma ascent velocity, bubble ascent velocity, magma viscosity, number of bubble nuclei, and gas solubility [e.g., *Slezin*, 2003; *Parfitt and Wilson*, 1995]. However, although well tested in the laboratory and with geophysical data [e.g., *Jaupart and Vergniolle*, 1988; *Vergniolle and Brandeis*, 1996; *Ripepe et al.*, 2001], models lack the constraints imposed by the actual physical conditions of the shallow-system magma through which the bubbles must rise, coalesce, and burst. Such information can be obtained from field sampling of the erupted products [e.g., *Corsaro et al.*, 2005; *Lautze and Houghton*, 2005, 2007, 2008; *Polacci et al.*, 2006, 2008, 2009; *Andronico et al.*, 2008; *Colò et al.*, 2010; *Pistolesi et al.*, 2011].

Stromboli (Figure 1) is an ideal field laboratory where such theories and relations can be tested. The active vent area is reasonably safe and easy to access, and the persistence of degassing and mildly explosive (Strombolian) activity provides a guaranteed target for multidisciplinary experiments designed to understand conduit processes and the genesis of basaltic explosions [e.g., *Ripepe et al.*, 2001, 2002; *Rosi et al.*, 2006; *Harris and Ripepe*, 2007a; *Scharff et al.*, 2008; *Landi et al.*, 2011; *Pistolesi et al.*, 2011]. The shallow system, the zone which spans the region between the level of large gas bubble formation and the magma free surface, is fed by highly viscous (~10^4 Pa s), partially degassed magma that contains, on average, 45–55 vol % of plagioclase, clinopyroxene, and olivine in equilibrium with a shoshonitic (SiO_2 ~52 wt %) residual melt [*Métrich et al.*, 2010]. Geochemical and isotopic analyses of Stromboli's products are consistent with the presence of a

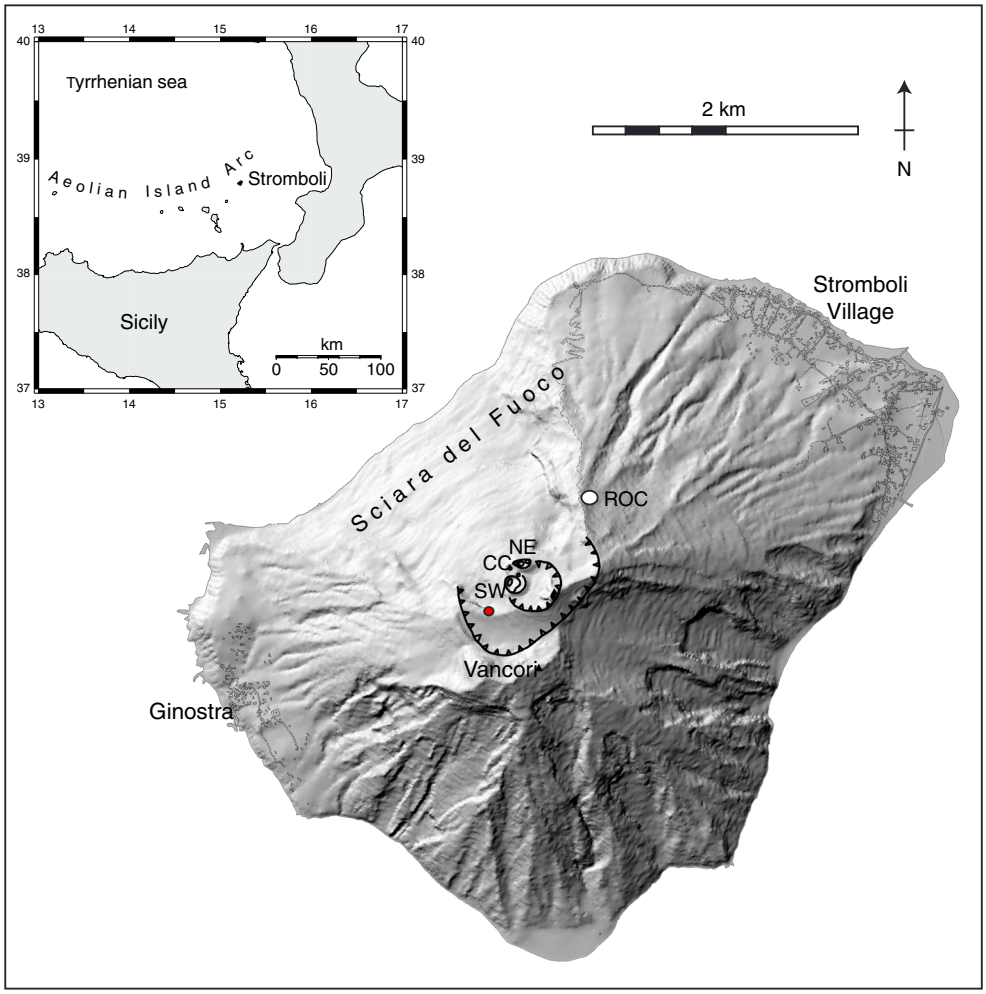

Figure 1. DEM of Stromboli Volcano, Italy. The crater area is shown, and the red spot is the sampling location for the two bombs. SW, CC, and NE refer to craters. ROC, Roccete station at ROC. The thermal camera was located 300 m southwest of the SW crater; the infrasonic and seismic array are located between SW crater and ROC.

polybaric, multireservoir system, comprising at least three different reservoirs [e.g., *Francalanci et al*., 2005; *Métrich et al*., 2010]. These are (i) a deep reservoir at 10–11 km, (ii) a shallower reservoir at 3.5 km [*Bertagnini et al*., 2003], and (iii) a conduit system that extends to the surface and which typically has its magma free surface at a depth between 20 m and 220 m [*Harris and Ripepe*, 2007a]. According to *Francalanci et al*. [2005], low-porphyritic (LP), light colored, volatile-rich pumices are only erupted from the deep reservoir during the most energetic eruptions. In contrast, highly porphyritic (HP), dark colored scoriae are erupted during normal explosive activity from the reservoir at 3.5 km. Often, these two end-members are mingled [*Andronico and Pistolesi*, 2010; *Pistolesi et al*., 2011; *Andronico et al*., 2013] and, recently, ash fragments of LP magma have been found in the products of normal activity [*D'Oriano et al*., 2011].

In terms of textural features, the HP scoriae have a population of spherical to subspherical (0.1 to 3 mm) vesicles and a sparser population of large vesicles with diameters of up to 10 mm. The entire vesicle population has a number density ranging from 10^2 to 10^4 mm^{-3} [*Lautze and Houghton*, 2005, 2007, 2008; *Polacci et al*., 2006, 2008, 2009; *Colò et al*., 2010]. All of these authors agree that these features have resulted from processes operating in the shallow conduit system. This shallow system is located above the convective overturn of vesicular magma which rises through the conduit, degasses, and then sinks back down as denser material [*Allard et al*., 1994; *Harris and Stevenson*, 1997; *Burton et al*., 2007].

Stromboli's normal activity consists of repeated explosive events from the main craters (i.e., NE, Central Crater, and SW), each lasting a few seconds to tens of seconds and which can be subdivided into ballistic-dominated

or ash-dominated explosive events [*Patrick et al*., 2007]. They are characterized by jets of gas and incandescent magma fragments that generally attain heights of 100–200 m, have typical exit velocities in the range 2 m s^{-1} to 100 m s^{-1}, and involve dense rock equivalent masses of 10^3 – 10^4 kg [*Blackburn et al*., 1976; *Chouet et al*., 1974; *Ripepe et al*., 1993; *Patrick et al*., 2007; *Harris et al*., 2013]. Recent studies show that maximum ejection velocities may be as high as 200–300 m/s [*Delle Donne and Ripepe*, 2012; *Taddeucci et al*., 2012] and are associated with a leading spray of lapilli-sized fragments that appear to be carried by the gas phase [*Harris et al*., 2012]. These explosions have been explained in terms of generation, ascent, and bursting of large gas slugs at the magma free surface [*Blackburn et al*., 1976; *Vergniolle and Brandeis*, 1996]. Two main models have been proposed to explain generation of the slugs: a collapsing foam model and a rise rate-dependent model [*Parfitt*, 2004, and references therein]. In the collapsing foam model, an accumulation of gas bubbles builds a foam trapped by some constriction in the conduit system. Upon reaching a critical thickness, the foam collapses to generate the gas slug, which enters and ascends the final section of the conduit to burst at the magma free surface [*Jaupart and Vergniolle*, 1988, 1989; *Vergniolle and Jaupart*, 1990]. In the rise rate-dependent model, the rise rate of the magma is relatively slow so that the bubbles have time to grow and coalesce to generate the slug [e.g., *Wilson*, 1980; *Parfitt and Wilson*, 1995]. In addition, the volcano is characterized by persistent degassing activity driven by small (<0.5 m in diameter) gas bubble bursting every 1–2 s due to overpressurized bubbly flow regime [*Ripepe et al*., 1996; *Harris and Ripepe*, 2007b]. This puffing style of activity appears to dominate activity in the central part of the system (i.e., activity at the central crater), with explosions characterizing the marginal zones (i.e., the SW and NE craters).

Geophysical measurements at Stromboli have typically been framed in the context of these two models [e.g., *Vergniolle et al*., 1996; *Ripepe et al*., 2001]. For example, seismic events associated with Stromboli's normal activity are characterized by a first arrival of a low-frequency (very long period, VLP) component (1–3 Hz), followed by a high-frequency (3–7 Hz) component [e.g., *Braun and Ripepe*, 1993; *Chouet et al*., 1999]. The source of the VLP signal is very stable and has been located at a depth of 220–300 m [*Chouet et al*., 1999, 2003]. These seismic events have been related to the generation of the gas slug [*Ripepe et al*., 2001; *Chouet et al*., 2003] or to a change in conduit inclination that can induce a change in regime to bubbly flow [*James et al*., 2004]. The high-frequency component is related to the explosion itself [*Ntepe and Dorel*, 1990]. In the classic model, the sound is caused by the bubble burst [*Vergniolle and Brandeis*, 1996; *Vergniolle et al*., 1996], followed by emission of the fragments at the vent to give a thermal signal [*Ripepe et al*., 2001, 2002; *Harris and Ripepe*, 2007a]. The general assumption is that the slug has to pass through a conduit filled with homogeneous magma to burst freely at the magma-air interface and that the geophysical signals should follow in a predictable and calculable way.

In June 2008, we collected two decimetric-sized bombs from an explosion that was also recorded using thermal video and an array of infrasonic and seismic sensors. The idea to study the bomb component of the explosion arose from the fact that while many normal explosions at Stromboli are dominated by this coarse component [*Patrick et al*., 2007], it is rarely sampled. We thus wanted to check if the textural signature of these large samples was identical to the lapilli-sized scoria more commonly described in the literature. Textural variations were quantified for each sample, including vesicle content, vesicle size distribution, phenocryst, and microlite crystal content. The glass chemistry was also analyzed, and the rheology of the samples measured. These physical data enabled us to define the magma conditions across the uppermost portion of the conduit, i.e., in the region of the magma-air interface where the bubble should burst. This information allowed us to connect the magma conditions to the accompanying geophysical signals and emission dynamics, and it led us to develop an integrated model that incorporates chemical and rheological heterogeneity within the conduit.

2. Setting and Methods

2.1. Activity

Sampling was carried out on the western flank of the SW crater, on the upper Sciara del Fuoco (Figure 1) on 3 June 2008. Seismic tremor was relatively strong during sampling, and gas puffing from the Central Crater was intense, reaching 23 Pa (compared with normal values of 30 Pa recorded at Roccete station, ROC, [*Lacanna and Ripepe*, 2013]) and was characterized by spattering episodes. By the standards of normal activity at Stromboli, the intensity of explosions, in particular those occurring at the SW Crater, were moderate-to-high.

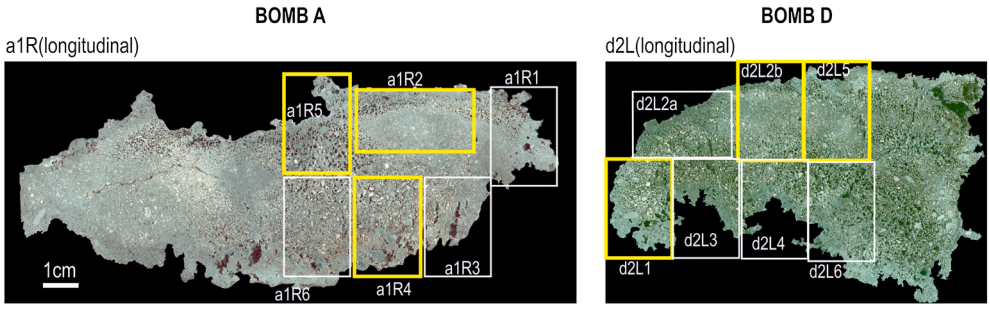

Sample		ρ gr cm^{-3}	Ves %
Bomb A	a1cL	2.0	32.0
	a1R	1.6	46.3
	a2	1.8	37.5
	b	1.7	42.3
	c	1.6	44.3
Bomb D	d2cR	1.5	50.5
	e1	1.4	51.0
	e2	1.4	51.8

Figure 2. The longitudinal and transverse parts of bomb A are a1R and a1cL, while the longitudinal and transverse cut parts of bomb D are d2L and d2cR, respectively. The white and yellow boxes locate the 24 thin sections, with the yellow ones indicating the thin sections chosen for SEM analyses. In the table, measured densities (ρ) and vesicularities (Ves) measures are listed. Different letters refer to the different pieces into which bombs were cut to calculate density values. "L" and "R" mean the left or the right face.

SW Crater activity was fed by a single 1–2 m wide vent, which emitted gas-rich bursts of bombs and lapilli to heights of 170–420 m, causing bombs to escape the ~80 m wide crater and land on the west (outer) flank of the crater, where they could be sampled in moderate safety (Figure 1).

2.2. Sampling and Sample Preparation

The two bombs were collected during an explosion at 11:11 (all times are GMT) on 3 June 2008. Each was 15 cm long, was emitted during a normal explosion from Stromboli's SW Crater, and came to rest on the upper Sciara del Fuoco (see Figure 1) ~300 m SSW of the vent. Both bombs were quenched by pouring water on them, allowing us to preserve their pristine texture and chemistry and to limit postfragmentation expansion. The explosion was also captured using a thermal camera (a FLIR Systems S40), as well as by the infrasonic array and seismic network maintained by the University of Firenze (Florence, Italy).

The two bombs (named A and D) comprised a main fragment "a", and two smaller pieces "b" and "c" for bomb A, and a main fragment "d", and two smaller pieces "e" and "f" for bomb D (Figure 2). Both bombs were sectioned longitudinally (a1R and d2L, Figure 2) and transversely (a1cL and d2cR, Figure 2). Because of their textural heterogeneity, 24 thin sections were prepared, from which 12 were chosen for higher magnification analyses (yellow boxes in Figure 2). Fragment $^{2}a^{2}$ (bomb A) was cut longitudinally, so we obtain portion a1 and a2. Portion a1 allowed us to examine the two bomb-scale sections, $^{2}a1R^{2}$ and $^{2}a1L^{2}$. Next, the $^{2}a1R^{2}$ part was cut transversely to generate two further sections: $^{2}a1cL^{2}$ and $^{2}a1cR^{2}$. Fragment $^{2}d^{2}$ (bomb D) was longitudinally cut and two sections, $^{2}d2R^{2}$ and $^{2}d2L^{2}$, were obtained. Subsequently, the $^{2}d2L^{2}$ fragment was cut transversely to provide two further bomb-scale sections, $^{2}d2cR^{2}$and $^{2}d2cL^{2}$. Finally, fragment $^{2}e^{2}$ was cut into two halves.

2.3. Density and Textural Measurements

The method of *Houghton and Wilson* [1989] was used to obtain sample bulk density. The dense rock density of fragments a2 and b from bomb A was measured by helium pycnometry at Washington University in St. Louis. About 22 g of fine powder was used for each, and the results were 2957 and 2948 kg m^{-3}, respectively, in agreement with the values found by *Pistolesi et al.* [2011]. Because of the size of the bombs and their

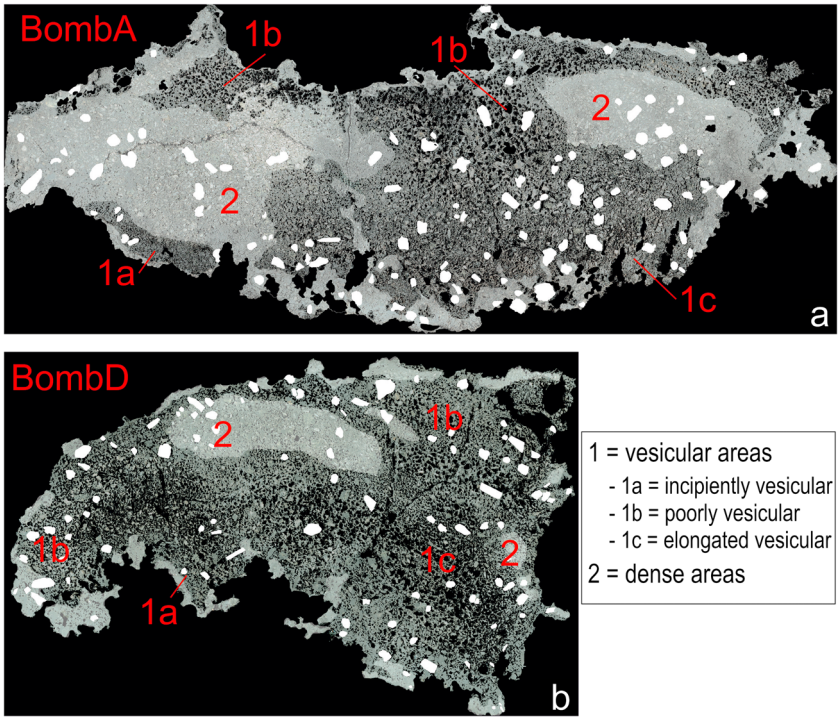

Figure 3. Bombs (a) A and (b) D (scale in Figure 2). Black = vesicles; white = phenocrysts; light grey area = dense areas; and dark grey areas = vesiculated areas.

heterogeneous nature (they contained both dense and vesicular zones in close proximity), we completed bulk density measurements for multiple samples of each bomb (see Table in Figure 2).

Next, the largest vesicle populations at the sample scale were imaged using a desktop scanner, either by scanning the thin section or the sectioned sample itself (Figure 3). Subsequent larger magnifications (e.g., at magnifications of 25×, 100×) were captured through scanning electron microscopy (SEM), in backscattered electron imaging mode, using chemical contrasts (Figure 4). The images were used as inputs into a MATLAB-based program named "Fast Object Acquisition and Measurement System" to yield various parameters that describe the spatial arrangement, as well as the size and number, of vesicles in the samples. *Shea et al.* [2010] details this image analysis strategy, as well as the stereological assumptions adopted. Results for both the bulk sample, and each texture observed in each bomb, are given in Table 1.

Finally, we calculated the percentage of crystals in two dimensions and adjusted the results to a vesicle-free basis. We then applied a spherical shape assumption to generate a qualitative sense of their size distribution, as given in Figure 5, while the percentage of phenocrysts and microlites were calculated using Image J (Table 1).

2.4. Chemistry

Electron microprobe analyses of glass compositions were determined with the University of Hawaii five-spectrometer Cameca SX-50 electron microprobe using SAMx automation. The operating conditions were a 10 μm spot size, 15 kV accelerating voltage, and 10 nA beam current. Peak counting times were 30 s for all elements except for potassium, which was measured for 90 s. Sodium was analyzed first to minimize its loss. Accuracy was checked on glass standards VG-2 and A-99 (basalts), and the raw data were corrected using ZAF-PAP procedures [e.g., *Reed*, 1993]. Results reported in Table S1 in the supporting information are averages of 12 spot analyses. Additional analyses were conducted using a CAMECA SX 100 electron microprobe at the Laboratoire Magma et Volcans (Clermont-Ferrand) facility with operating condition of 5–10 μm spot size, 15 kV accelerating voltage, and 4–8 nA beam current. Compositions of samples used in rheology experiments were analyzed using the JEOL JXA-8200 microprobe at Washington University in St. Louis, with a 15 kV

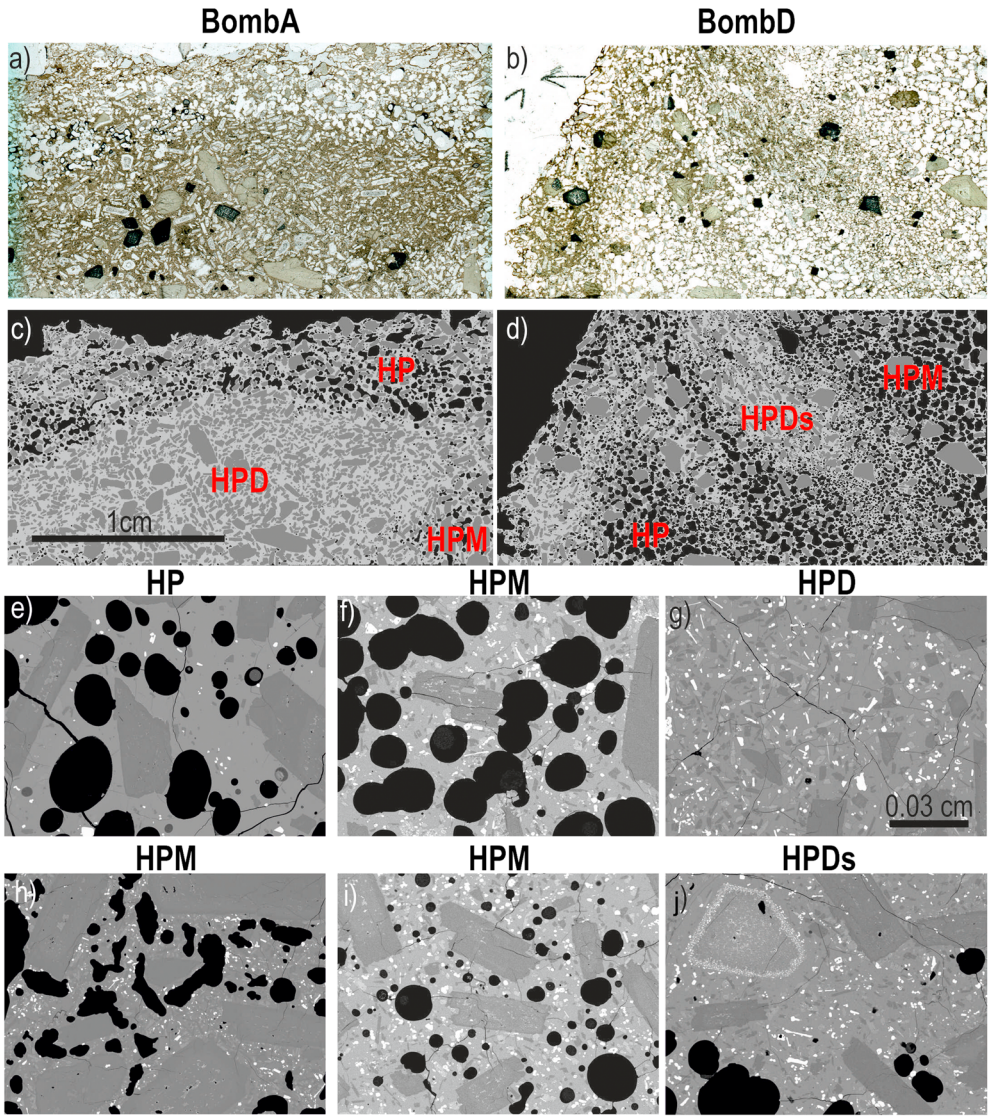

Figure 4. (a and b) Thin section of a portion of bomb A and D in which dense and vesiculated areas are well visible. The dense areas are characterized by oxidized olivines (crystals in black). (c and d) The same processed thin sections are shown: dark = vesicles; light grey = glass; and dark grey = crystals. For the thin sections the same scale is reported in Figure 4c. (e–j) Backscattered SEM (BSE) images magnified 25X show the different textures. See text for explanation. HP, HPM, HPD, and HPDs are textural facies defined in section 3.2. In Figure 4g the scale is reported for all the SEM images.

accelerating voltage and either 10 nA or 25 nA beam current with either a 1 μm or 5 μm spot size, depending on the session. Peak counting times were 60 s for all elements; again, sodium was always analyzed first.

2.5. Rheological Experiments

The rheology of the bomb material was investigated using four different approaches. First, we measured the rheology of pristine bomb material directly using a Theta Industries Rheotronic 1000 parallel-plate viscometer, as described by *Whittington et al.* [2009]. A ~8 mm diameter cylindrical core of bomb fragment a1cL was drilled using a diamond core bit, cut to ~10 mm length using a diamond wafer saw, and polished to smooth parallel faces using carbide grit paper. The core was subjected to uniaxial compression with a 1.5 kg load at temperatures of between 895°C and 985°C. Viscosity was calculated from the ratio of the applied stress to the observed strain rate, assuming constant volume (a reasonable approximation for the small finite strains

Table 1. Summary of Textural Features for Each Bomb[a]

Samples		Texture	Ves (%)	N_i	N_ves	N_ctx	Ctx_{corr} (%)	$Pheno_{corr}$ (%)	$\mu lites_{corr}$ (%)	N_V (mm^{-3})	N_{Vcorr} (mm^{-3})
						Bomb A					
Face_a1R	a1R2	Mixture	20	17	329	3110	51	47	8	684	1768
(longitudinal)		HP	23	10	588	735	42	39	4	803	1671
		HPD	1	9	57	2643	55	49	11	515	1013
	a1R4	HPM	35	19	803	3158	58	52	13	1784	5508
	a1R5	HPM + HP	41	13	466	1208	55	52	6	1342	4160
Face_a1L	a1cL1	Mixture	39	20	1196	2674	40	37	5	1360	3545
(trasversal)		HP	31	7	423	312	40	39	2	1167	2773
		HPM	44	13	523	1757	41	37	7	1682	4980
	a1cL3	Mixture	36	10	165	2169	46	39	11	726	1725
		HP	48	7	169	645	41	39	4	645	1995
		HPD	9	4	82	1278	50	39	19	866	1517
	a1cL4	Mixture	21	17	1851	6068	55	46	17	6311	15146
		HPM	26	12	839	3688	56	47	17	7015	18639
		HPD	9	6	482	3110	54	44	19	5406	10600
		Minimum	1	4	57	312	40	37	2	515	1013
		Maximum	48	20	1851	6068	58	52	19	7015	18639
		Mean	27	12	570	2325	49	43	10	2165	5360
		ST	14	5	487	1522	7	5	6	2266	5518
						Bomb D					
Face _d2L	d2L1	Mixture	32	19	729	3569	51	47	8	665	1852
(longitudinal)		HP	22	4	115	99	49	48	1	518	1270
		HPM	31	16	635	3438	52	47	9	694	1867
	d2L2b	Mixture	30	18	1366	4324	54	47	13	2823	7079
		HPM	41	9	496	1531	56	52	9	4256	13268
		HPDs	20	10	508	2774	51	42	16	5376	10278
	d2L5	Mixture	37	18	1179	3925	48	41	11	1059	2891
		HPM	45	9	145	978	47	43	8	668	2093
		HPDs	25	10	1350	2811	46	37	15	1235	2695
Face _d2R	d2cR1	Mixture	32	19	688	6073	51	46	10	1591	4679
(trasversal)		HP	37	11	727	1196	53	50	5	930	3014
		HPDs	12	13	275	3261	48	40	13	1890	3660
	d2cR4	Mixture	46	19	763	4053	40	34	9	896	2653
		HP	54	4	76	161	31	29	3	533	1741
		HPDs	20	7	477	1451	46	39	12	772	1605
		HPM	57	10	687	2350	36	30	9	1097	3910
	d2cR5	HPM	45	19	574	3636	42	37	8	2896	8431
		Minimum	12	4	76	99	31	29	1	518	1270
		Maximum	57	19	1366	6073	56	52	16	5376	13268
		Mean	34	13	635	2684	47	42	9	1641	4293
		ST	13	5	387	1607	7	7	4	1408	3449

[a]The table shows the following, for each sample: textural facies (Texture), 2-D integrated vesicularity (Ves); number of images processed for each sample (N_i); number of vesicle and crystal analyzed for each sample, respectively (N_ves, N_ctx); vesicle-free percentage of crystals (Ctx_{corr}); vesicle-free percentage of phenocrysts ($Pheno_{corr}$); melt reference microlites ($\mu lites_{corr}$); total volumetric number density of vesicles referenced to whole clast (N_v); total volumetric number density of vesicles referenced to melt only (N_{vcorr}).

obtained: <4% shortening). The accuracy of the viscometer is about 0.06 log units for homogeneous glasses [*Whittington et al.*, 2009].

Second, we measured the viscosity of the homogeneous remelted liquid. A portion of bomb fragment a1cL was melted in a Pt crucible in a muffle furnace in air for 30 min at 1500°C and then quenched to glass. The superliquidus viscosity was measured using a Theta Industries Rheotronic 1600 rotating viscometer, at temperatures between ~1120°C and 1500°C, with an accuracy of about 0.02 log units, as described by *Getson and Whittington* [2007]. Four cores of remelted glass were drilled and polished, and parallel-plate data were collected in the temperature range ~680 to ~750°C and in the viscosity range ~10^9 to 10^{11} Pa s.

Third, in an attempt to bridge the gap between homogeneous melt and partially crystalline, vesicular magma, we heated each of the four cores used in the parallel-plate viscometer to a higher temperature (950 or 1000°C) where crystal nucleation would be rapid. The samples dwelled at high temperature for up to 60 min, before their viscosity was measured. This was followed by rapid cooling and characterization of crystal content by SEM imaging.

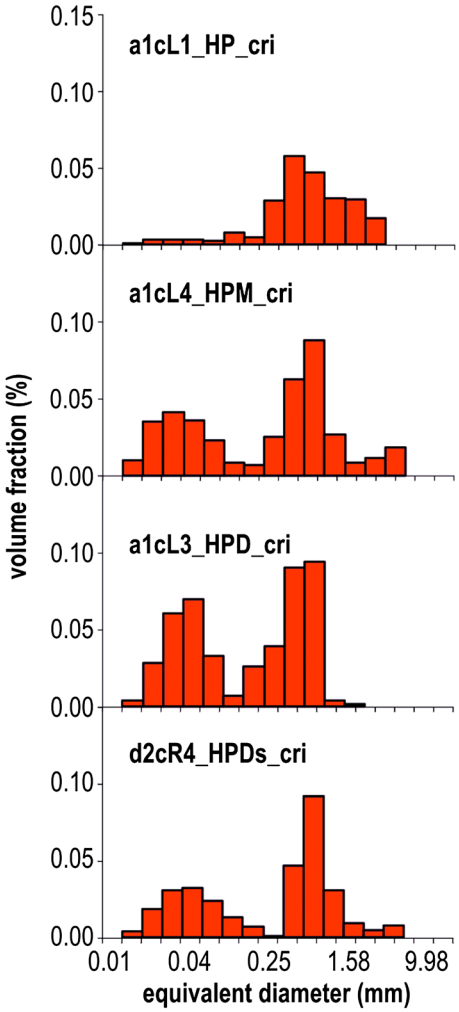

Figure 5. Qualitative crystal size distributions (CSDs) of the total crystal content in the different texture facies recognized in bomb A (a1) and in bomb D (d2) and defined in section 3.2.

Finally, we took two cores from each of the three bomb fragments and deformed them in the parallel-plate viscometer at a constant temperature of 985–988°C, cycling the applied uniaxial stress up and down through three different amounts. The resulting stress-strain rate curves can be extrapolated to zero strain rate in order to estimate the yield strength (if any) at this temperature. The apparent viscosity increases through time due to crystallization during the experiment, potentially allowing the onset or change in yield strength to be observed.

2.6. Geophysical Data

The explosion (Figure 6a) was captured using a thermal camera and an infrasonic and seismic array (Figure 6b). As described by *Vanderkluysen et al*. [2012], thermal video of the eruption was recorded using a tripod = mounted FLIR Systems ThemaCAM™ S40. The camera was located 300 m to the SW of the SW crater and acquired imagery at a rate of six images per second. Images were 320 × 240 pixels in size, with each pixel having a 1.3 mrad instantaneous field of view, which equates to 39 cm wide pixels over our line of sight distance. Pixels were corrected for oblique viewing effects, and the trajectories of 48 bombs were tracked, including the sampled bombs. For each bomb, this allowed us to extract bomb exit velocity, height, and distance (i.e., the distance between the launch and landing point). The eruption was also recorded using a pressure sensor, a seismometer, and a thermal infrared thermometer whose outputs were sampled at 55 Hz. These instruments were located at station ROC, 650 m NE of the center of the SW crater (Figure 1).

3. Results

3.1. The Eruption

The VLP seismic event, which is typically associated with generation and/or ascent of the slug [e.g., *James et al*., 2004], began at 11:10:49 and occurred at a depth of 450 m below the vent (Figure 6c). Onset of the infrasonic signal, due to bursting of the slug at the free surface, was recorded at 11:11:03, with first emission of ejecta from the vent being recorded by the radiometer at 11:11:02 (Figure 6c). The emission ended at 11:11:23, having lasted 22 s. From the thermal camera data we obtained a range of exit velocities for the bombs of 27–67 m s^{-1}, with a mean of 48 m s^{-1} and a standard deviation of 10 m s^{-1}. Bombs reached maximum heights of 155 m and landed at distances of between 9 and 71 m from the vent, their flight paths detailed by *Vanderkluysen et al*. [2012].

3.2. Qualitative Textural Observations

Both bombs are rich in heterogeneously distributed crystals. The phenocryst assemblage of olivine, plagioclase, and clinopyroxene is typical of Stromboli's HP dark scoria. From the rock scan, the 2-D percentage of phenocrysts with a long diameter > 2 mm is about 6% in bomb A and 4% in bomb D (Figure 3). The vesicle distribution is heterogeneous in both bombs, with a high concentration in areas 1a, 1b, and 1c (Figure 3a) and a low concentration in area 2 (Figure 3a). The vesicle-poor areas make up 44% of bomb A and 11% of bomb D.

Following the terminology of *Houghton and Wilson* [1989], we divided the vesicular areas into four types (Figure 3): type 1a: incipiently vesicular areas characterized by small vesicles (smaller than 0.5 mm), type 1b:

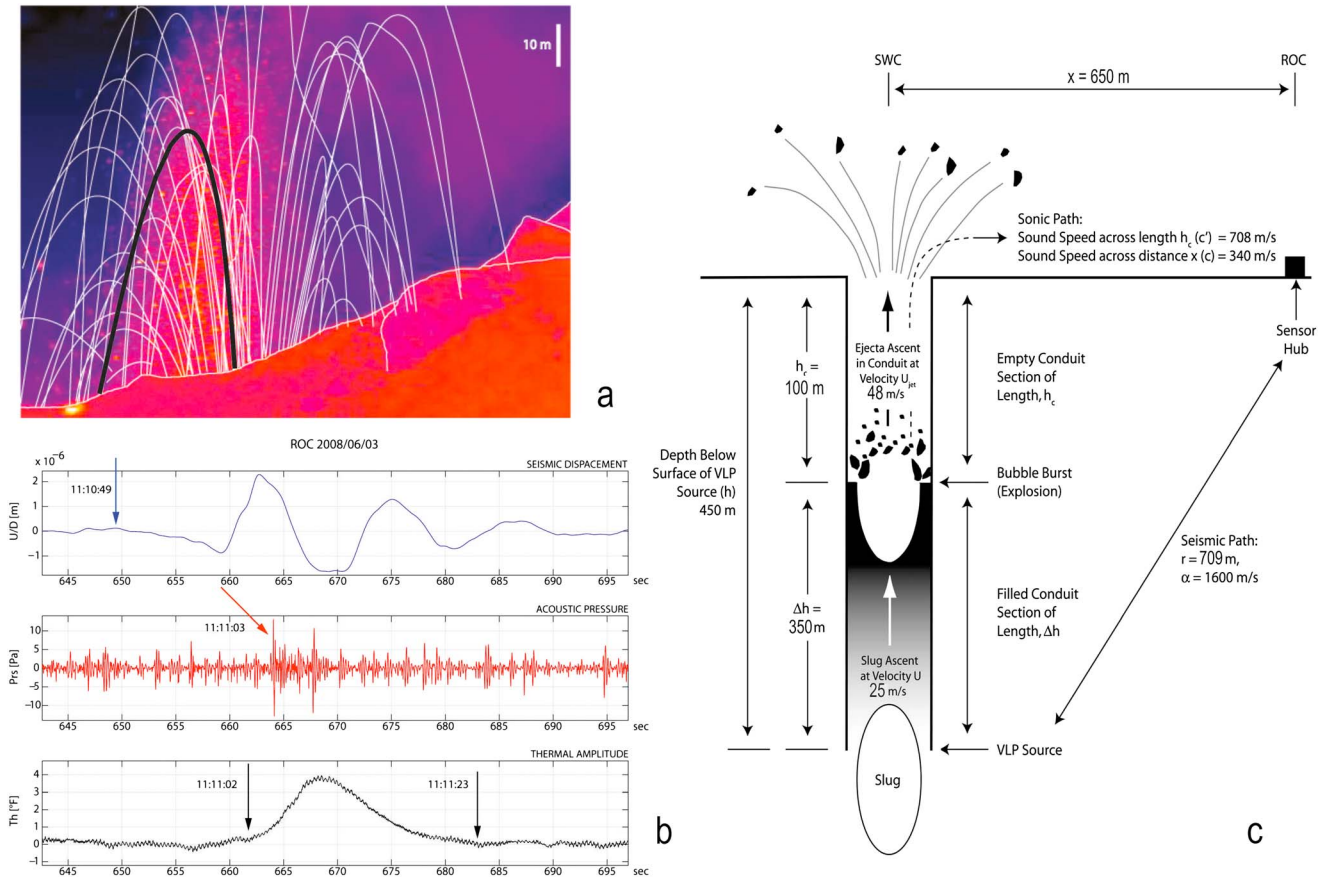

Figure 6. (a) Thermal image taken from ROC of the 6 June 2008, 11:11 GMT normal explosion at Stromboli dominated by a jet of bombs. The thick trajectory in black corresponds to bomb A. This bomb had an exit velocity of 45 m/s, reached a maximum height of 48 m, and came to rest 298 m from the vent. (b) (from bottom to top) Thermal, acoustic, and seismic signals acquired for the same explosion. (c) Schematic model for the shallow (above 300 m) system at Stromboli. The source is located at depth h below the surface and at depth Δh inside the magma column. The slug ascends distance Δh at velocity U to burst at the free surface at depth h_c. The cloud of fragments and gas then ascends the empty conduit length of distance h_c at velocity U_{jet}, to be emitted from the vent. All depths and velocities are set using the typical range in seismic-infrasonic-thermal delay times (reported in Figure 6b) for sensors colocated at distance x from the vent, with a range in fragment ascent velocity of 27–67 m/s. The diagram is modified from *Harris and Ripepe* [2007a].

poorly vesicular areas characterized by vesicles with diameters 1–2 mm, type 1c: poorly vesicular areas with elongated vesicles aligned perpendicular to the primary long axis, and type 2: dense areas with few vesicles.

Although these bombs were quenched, a few portions show the characteristic cooling thermal gradient [e.g., *Gurioli et al*., 2008] of small vesicles at the edge of the bomb, followed by larger vesicles toward the interior of the sample (see a1cL1 in Figure 2). However, centimeter-sized vesicles occur at the edges of both bombs, whereas millimeter-sized vesicles are organized into clusters in bomb A and into lenses in bomb D. The centimeter-scale vesicles have irregular shapes, with the long axis of the vesicle aligned perpendicular to the long axis of the bomb. Smaller vesicles are circular with rounded, nondeformed shapes. At higher magnifications it is possible to observe that the densest portions of each bomb are characterized by the highest content in microphenocrysts and microlites.

Based on these textural observations, we can define four main textural facies, as illustrated in Figure 4: HP facies: highly porphyritic, vesiculated regions (vesicularity types 1a and 1b) characterized by microlite-poor glass (Figures 4a, 4c, and 4e), HPM facies: highly porphyritic, vesiculated regions (vesicularity types 1b and 1c) characterized by microlite-rich glass (Figures 4f, 4h, and 4i), HPD facies: highly porphyritic, vesicle-poor regions (vesicularity type 2) characterized by microlite-rich glass (Figures 4a, 4c, and 4g), and HPDs facies: highly porphyritic, transitional facies between regions poor in vesicles and regions rich in rounded, small vesicles, usually smaller than 0.5 mm in diameter, of vesicularity type 1a, and characterized by microlite-rich glass (Figures 4b, 4d, and 4j).

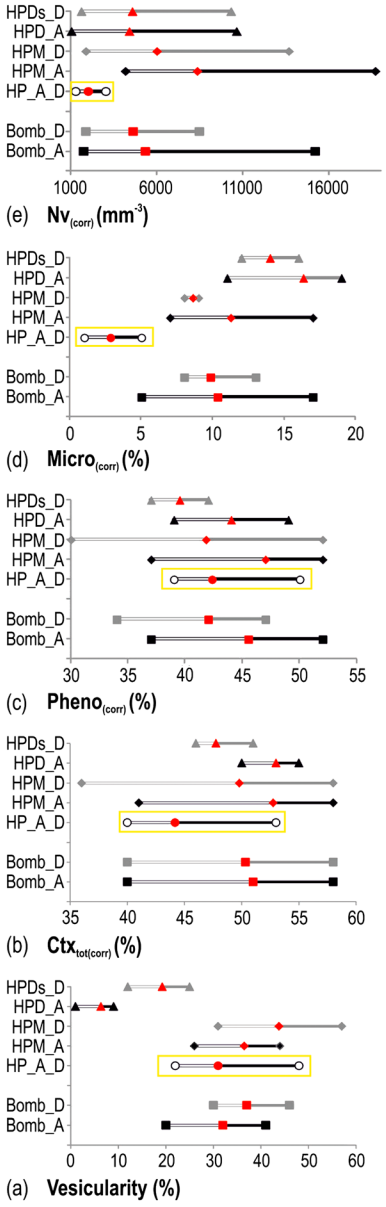

Figure 7. Average (in red), minimum and maximum values for six parameters from the two bombs as a whole (bomb_A and bomb_D) and from the different textural facies in each bomb: HP_A_D = HP facies in bomb A and bomb D; HPM_A and HPM_D = HPM facies in bomb A and bomb D; HPD_A = HPD facies in bomb A; HPDs_D = HPDs facies in bomb D. (a) Percentage of density-derived vesicularity = vesicularity (%); (b) vesicle-free crystal content = $Ctx_{tot(corr)}$; (c) vesicle-free phenocryst content = $Pheno_{(corr)}$ (%); (d) vesicle-free, microlite content = $Micro_{(corr)}$ (%); and (e) $Nv_{(corr)}$ (mm^{-3}).

The proportion of HP facies is quite low in respect to the HPM, HPD, and HPDs facies. All facies are, though, mingled and randomly distributed in the bombs. The HP facies lacks elongated or deformed vesicles and has a low content of small vesicles (30–40 μm in diameter, Figure 4e). The HPM facies has both large and small vesicles (Figures 4f, 4h, and 4i). The former are rounded (Figure 4i), but commonly also deformed, squeezing into spaces between the phenocrysts (Figure 4h). Instead, microlites puncture vesicles. The HPDs facies contains no millimeter-sized vesicles but instead has smaller, rounded, vesicles (Figures 4f, 4i, and 4l), particularly of the smallest vesicle size (30–40 μm in diameter, Figure 4f). The three microlite-rich facies are distinctive in that they contain phenocrysts of oxidized olivine (Figures 4a, 4b, and 4f) that are characterized by both oriented, and pervasive, nonoriented vermicular symplectite-like textures. All oxidized olivine phenocrysts have reaction rims (Figure 4f).

3.3. Quantitative Textural Measurements

Because of the heterogeneity of the two bombs, we quantified each texture in terms of density, vesicle size distribution, crystal content (phenocrysts versus microlites), and glass chemistry. Thus, we defined these parameters for the thin section as a whole, as well as for each facies apparent in the thin section (see Table 1). This allowed us to check whether the parental magmas of the four facies experienced (i) single or multiple vesicle nucleation and expansion events, (ii) the same degassing history, and/or (iii) the same residence time in the conduit before the explosion.

For the density measurements, we measured samples from both the densest and most vesicular portions of each facies. Bomb A has a greater proportion of denser regions than bomb D. As a result, samples from bomb A have densities between 1.6 and 2 g cm^{-3}, but samples from bomb D have homogeneous densities of around 1.4 g cm^{-3}. These values match those for bombs emplaced by major explosions [*Gurioli et al.*, 2013]. To quantify the microscopic textural variations, we analyzed several thin sections, including at least one from each textural facies observed (Table 1).

In Figure 5 we report the qualitative crystal size distribution (CSD). Although the spherical assumption is not corrected for, we use the distribution only to compare the different facies and to highlight the possible presence of different size populations. All of the facies are characterized by a main population of crystals larger than 100 μm, with the HPM, HPD, and HPDs facies also having a second, distinct, population between 0.10 and 100 μm. Therefore, we calculated (in 2-D) the percentage of phenocrysts (with a longest diameter > 100 μm) versus microlites (longest diameter < 100 μm), as given in Table 1. The microlite phases are oxides, pyroxenes, and plagioclase.

In Figure 7 we plot the average, minimum, and maximum values related to the vesicularity, content in crystals, and N_v (number of vesicles per unit volume) for the two whole samples (bombs A and D), as well as for the samples taken from each of the textural facies (Table 1). The vesicularity values from the image analyses agree well with the density variations found from measuring portions of the bombs (Figure 2). The HP facies is characterized by the widest range in vesicularity, 22–48%, with the HPM facies having the highest values (up to 57%) (Figure 7a). In contrast, the HPD facies is

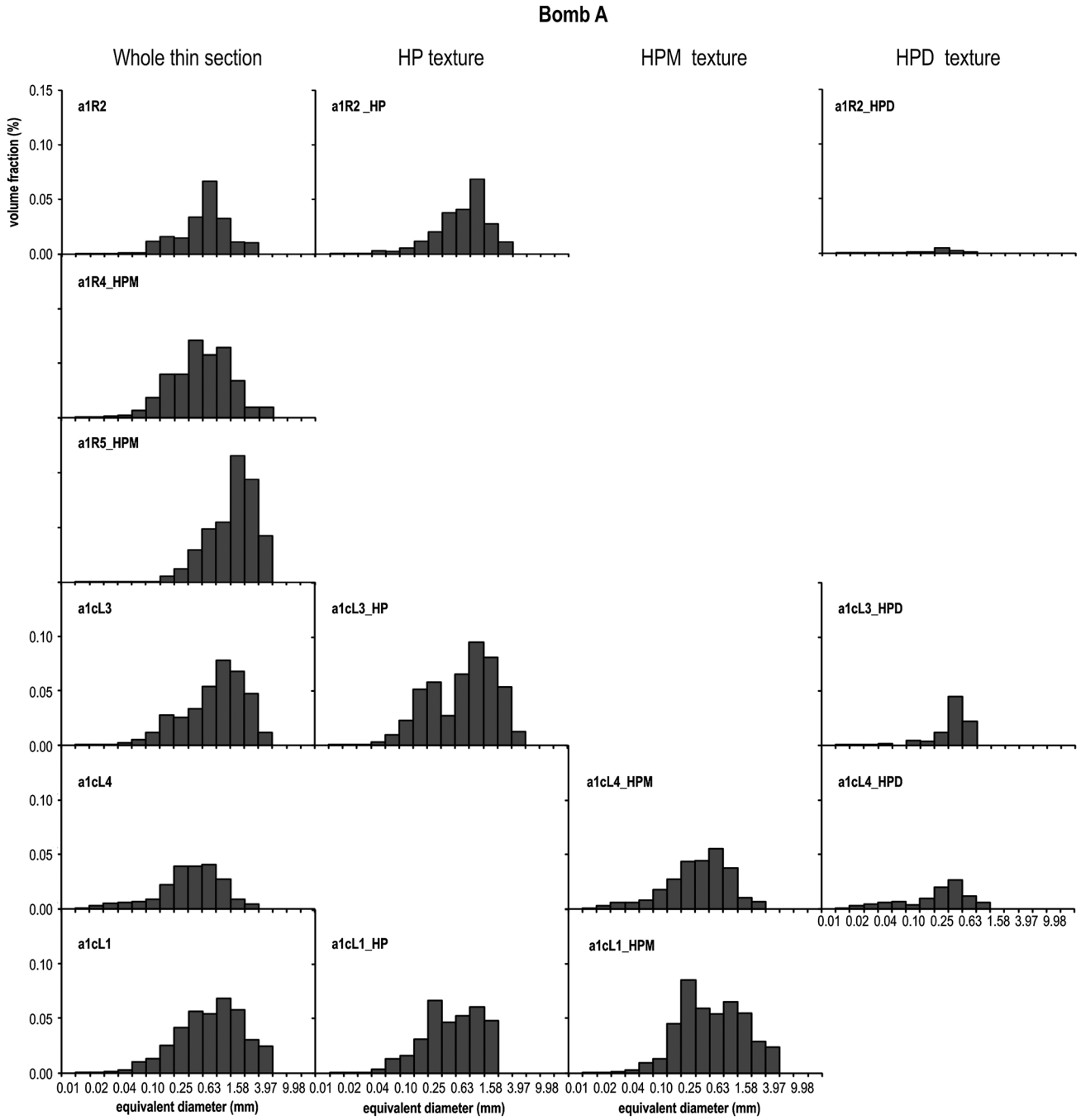

Figure 8. Distribution of vesicle sizes in bomb A as a function of volume fraction. The distributions are shown for the whole thin sections, as well as for the single textural facies recognized in each thin section

characterized by the lowest, and narrowest, vesicularity range, almost 0–9% (Figure 7a). The average crystallinity is the lowest in the HP facies, with the highest and lowest values in the HPM facies (Figure 7b). The range of values for phenocryst content is very wide for the HPM facies of bomb D but less so in the other facies (Figure 7c); facies HPDs has the lowest average. The HP facies has the lowest content of microlites (Figure 7d); the two dense facies show the highest averages (Figure 7d). In addition, the HP facies has the lowest average and narrowest range of N_v, whereas the other facies have much higher averages and very large ranges (Figure 7e).

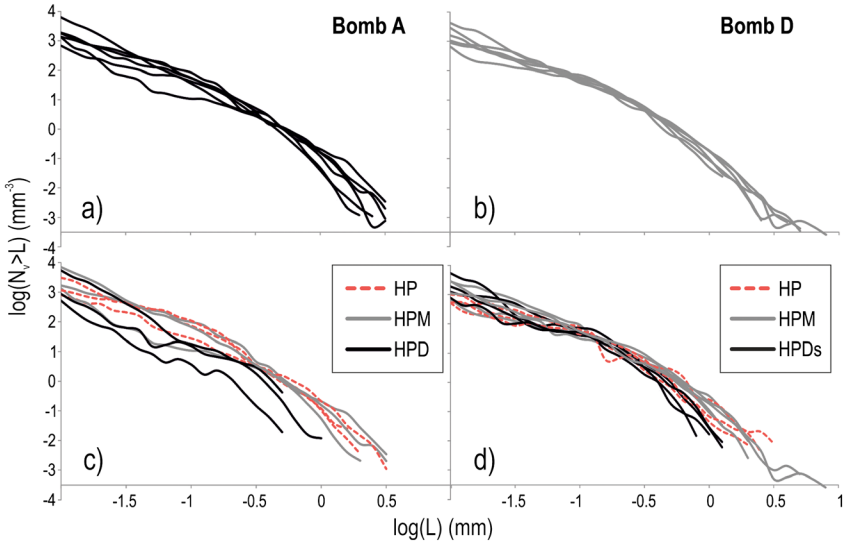

Figure 9. Number of vesicles greater than a given size (cumulative number density referenced to the melt volume) versus size on a log-log plot for (a) the whole thin sections in bomb A, (b) the whole thin sections in bomb D, (c) for the single textural facies recognized in each thin section of bomb A, and (d) for the single textural facies recognized in each thin section of bomb D.

The vesicle size histograms for the whole bomb (Figures 8) are characterized by unimodal distributions, despite the presence of the different textural facies. They are also negatively skewed. In bomb A only sample a1R2 has values that are relatively evenly distributed on both sides of the mean (Figure 8), and only two samples of bomb D (d2L1 and d2cR5, Figure S1) show clear signatures of expansion (positive skewing). When examining the different facies, the plots show more complex distributions. Facies HP, in bomb A, is unimodal and negatively skewed (a1R2_HP, a1cL1_HP, Figure 8) or bimodal with a main mode at 0.63 mm and a second mode at 0.25 mm (a1cL3_HP, Figure 8). In bomb D the HP distribution is characterized by a clear signature of expansion (d2L1_HP, d2cR1_HP, Figure S1). HPM, in bomb A, is characterized by a unimodal distribution, with a slightly positive skew in a1cL1_HPM (Figure 8),but a negative skew for the other sample. In bomb D, the HPM texture has a bimodal distribution in d2L2_HPM (Figure S1), with a main mode at 0.63 mm and a second, minor, mode at 0.10 mm. Sample d2cR4_HPM is characterized by a peculiar distribution, complicated by an expansion signature at 6.29 mm and a population of tiny vesicles with a mode at 0.06 mm. Only in two thin sections could we extract both facies HP and HPM (a1cL1 and d2L1, Figure 8 and Figure S1). In both cases the distributions are similar, although facies HPM has a more abundant population of large vesicles. Finally, the HPD and HPDs facies are those characterized by the most developed skew toward the fine fraction (Figures 8 and S1).

In Figure 9 we compare the whole-bomb cumulative volume fraction data and those obtained from single facies. For the whole-bomb data (Figures 9a and 9b), distributions are similar, especially in bomb D. However, the different characteristics of each textural facies are evident in Figures 9c and 9d. See, for example, the difference between the HP and HPM facies, with HPM showing the strongest signature of expansion (especially in bomb D). In contrast, the HPD and HPDs facies lack vesicles larger than 2 mm but have among the highest contents of small vesicles.

3.4. Chemical Results

Chemical analyses were conducted on the glassy matrix (free of microlites) for the HP and HPD facies (samples a1R2, d2L2b, Table S1) and for the HPM and HPDs facies (d2R4 sample, Table S1). Several spot analyses were made from the HP areas into the HPD areas in the two bombs (Figures 10a and 10b and Table S1). In bomb A, there is a correlation between increasing silica and increasing microlite content of the glass matrix along this traverse (Figure 10a). A plot of CaO/Al_2O_3 versus K_2O content (Figure 10c) shows that the variation in potassium is consistent between the HP dark scoriae (orange area in Figure 10c) and the HP facies isolated in the two bombs (triangles in Figure 10c). In contrast, the variation in K is well outside the orange area for the

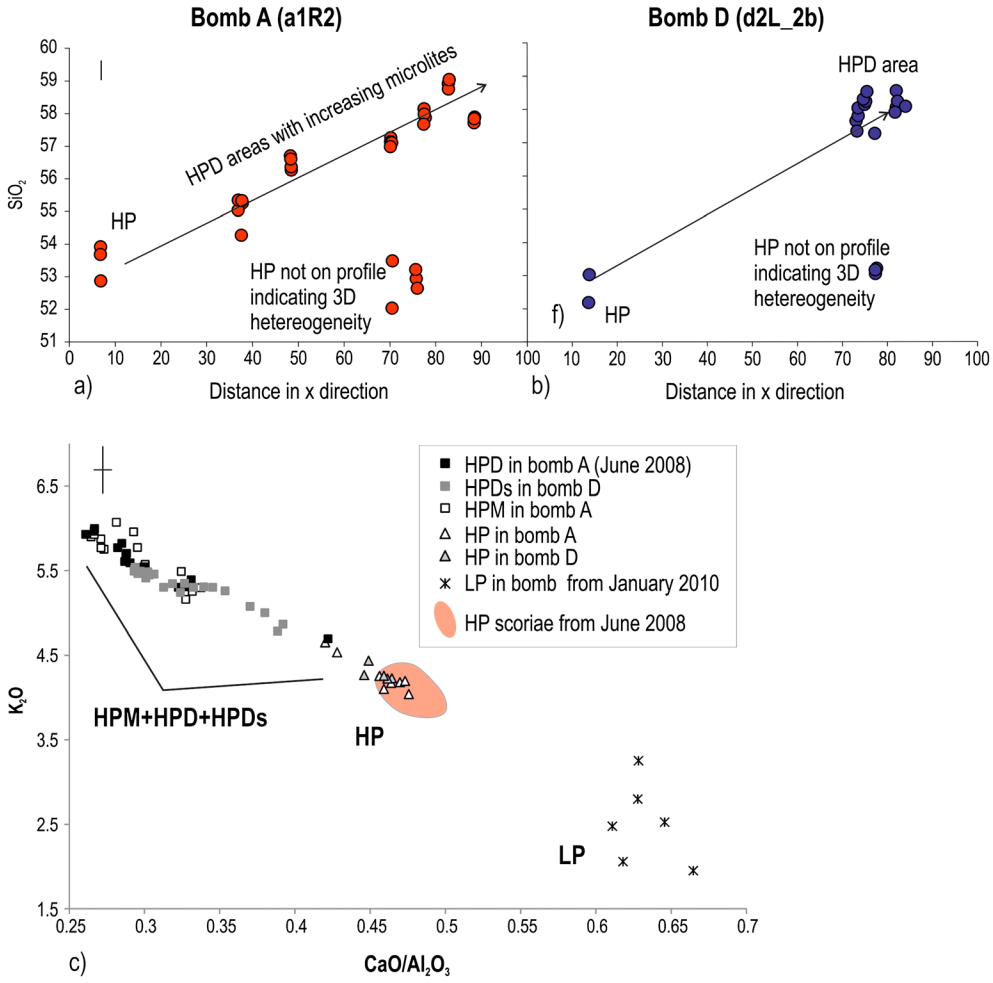

Figure 10. (a and b) Distance variation in *x* coordinate (in micron) in the probe versus SiO_2 content of glass for the two bombs a1R2 (red dots) and d2L_2b (blue dots), (c) CaO/Al_2O_3 ratio of glass versus K_2O content of glass.

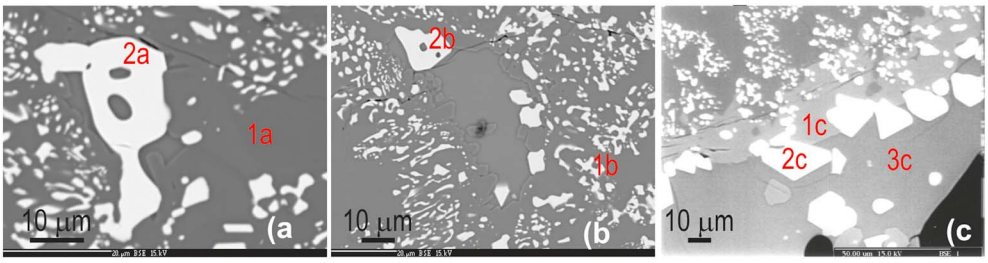

Points	SiO_2	TiO_2	Al_2O_3	Cr_2O_3	FeO	MnO	MgO	CaO	Na_2O	K_2O	P_2O_5	Total
1a = olivine	40.40	0.02	0.02	0.00	9.85	0.53	48.05	0.12	0.00	0.00	0.00	98.99
2a = oxide	0.15	1.24	3.22	0.01	78.93	0.50	7.58	0.02	0.02	0.00	0.00	91.66
1b = oxide	1.95	0.88	3.00	0.01	77.31	0.55	8.68	0.09	0.01	0.01	0.00	92.48
2b = oxide	0.10	0.99	3.21	0.02	78.53	0.52	7.50	0.02	0.00	0.02	0.00	90.92
1c = ring	49.98	1.03	3.88	0.01	7.40	0.36	16.08	20.55	0.45	0.01	0.00	99.76
2c = oxide	0.13	3.30	4.73	0.00	74.10	0.63	9.19	0.12	0.02	0.03	0.00	92.24
3c = glass	54.63	1.28	15.39	0.00	4.53	0.36	2.47	3.89	3.62	6.07	0.93	98.17

Figure 11. Olivine analyses in bomb A. (a–c) BSE probe photos of an olivine, the symplectites inside the olivine, the rim of pyroxenes at the edge of the crystal, and the glass wetting the olivine, respectively.

Table 2. Parallel-Plate Viscosity Data

Segment	T (°C)	Log η (Pa s)	
	a1cL Bulk Rock		
6	918.4	10.50	
7	948.7	10.29	
8	969.1	10.05	
9	984.1	9.92	
10	978.9	10.29	
11	945.4	10.88	
12	927.6	11.58	
14	895.1	12.20	
Segment	T (°C)	log η	notes
	Remelt core #1		
1	753.3	8.81	gl[a]
2	734.8	9.38	gl[a]
3	714.7	10.06	gl[a]
4	695.3	10.73	gl[a]
	Ramp to 1000°C, dwell for 60 min		
4	910.4	10.31	xtl[b], 2[c]
5	909.3	10.68	xtl[b], 2[c]
6	930.3	10.83	xtl[b], 2[c]
8	954.9	11.01	xtl[b], 2[c]
9	994.9	10.55	xtl[b], 2[c]
10	967.5	11.10	xtl[b]
	Remelt core #2		
1	748.4	9.02	gl[a]
2	729.6	9.61	gl[a]
3	709.4	10.44	gl[a]
	Ramp to 1000°C, dwell for 0 min		
9	749.3	10.73	xtl[b]
10	769.2	10.91	xtl[b]
11	769.0	11.08	xtl[b]
4	827.6	10.40	xtl[b], 2[c]
5	809.4	10.98	xtl[b], 2[c]
6	768.6	11.80	xtl[b], 2[c]
	Remelt core #3		
2	725.5	9.37	gl[a]
3	703.2	10.28	gl[a]
4	682.4	11.09	gl[a]
8	736.6	9.15	gl[a]
	Ramp to 950°C, dwell for 0 min		
13	803.9	9.18	xtl[b]
14	784.0	9.79	xtl[b]
15	763.9	10.39	xtl[b]
16	743.8	10.99	xtl[b]
17	723.9	11.66	xtl[b]
	Remelt core #4		
2	736.5	9.05	gl[a]
3	717.1	9.68	gl[a]
4	698.2	10.33	gl[a]
5	678.8	11.05	gl[a]
	Ramp to 950°C, dwell for 60 min		
15	958.4	10.30	xtl[b]
17	973.3	10.16	xtl[b]
18	993.4	9.91	xtl[b]
19	944.2	11.14	xtl[b]
20	929.3	11.62	xtl[b]
21	908.6	11.84	xtl[b]

[a]gl = measurement on glassy core (melt).
[b]xtl = after high temperature annealing, some crystals (c.f. Figure 10c).
[c]2 = measurements collected during a subsequent run on another day, after cooling to room temperature.

other three facies rich in microlites (squares in Figure 10c). However, the data follow a linear trend from the HP to the microlite-rich facies (Figure 10c).

Oxidized olivine phenocrysts in the HPM portion of the d2R4 thin section were analyzed, as well as oxides both inside and outside the olivine. The results show that the olivine is richer in magnesium with respect to that of the HP magma [e.g., *Francalanci et al*., 2005; *Landi et al*., 2004]. The olivine is similar to the altered olivine described in lava by *Cortés et al*. [2006] and found within lithic blocks ejected during the 2007 paroxysmal event by *Del Moro et al*. [2013]. In the olivine shown in Figure 11, the oxides are all magnetite; the external oxides are richer in titanium than the internal oxides (Figure 11). The alteration rind of the olivine is clinopyroxene (Figure 11).

3.5. Rheology Results

The results of the various viscosity experiments are given in Tables 2 and 3 and plotted in Figure 12. The rock core initially showed only a slight decrease in apparent viscosity as the temperature was increased from 918 to 984°C (Figure 12a). As the temperature was reduced to 895°C, the viscosity increased at a more typical rate, similar to that observed for the remelted material. We interpret the increase in apparent viscosity over time as due to ongoing crystallization of the interstitial melt at the subliquidus conditions of measurement.

For the remelted material, the four different cores used to obtain the parallel-plate data give similar results, although their viscosity is different by more than measurement uncertainty, perhaps suggesting minor differences in oxidation state in cores drilled at different distances from the melt-air interface. The concentric cylinder data show a smooth increase in viscosity as temperature decreases from ~1500 to ~1200°C (Figure 12a). However, the three lowest temperature points deviate sharply toward higher apparent viscosities. This indicates that the liquidus was crossed between 1218 and 1191°C. On heating back to 1500°C, the viscosity matched that measured earlier, indicating that all crystals remelted quickly. The points below the liquidus fall along a line that extrapolates close to the first parallel-plate data measured on the rock core, consistent with a slightly smaller crystal fraction in the magma at 1120°C than in the rock core. The bomb may therefore have an effective quenching temperature close to 1100°C.

Table 3. Concentric-Cylinder Viscosity Data

Segment	T (°C)	Log η (Pa s)	
5	1500.9	0.73	
6	1461.6	0.88	
7	1413.0	1.10	
8	1364.3	1.35	
9	1315.8	1.61	
10	1267.0	1.92	
11	1218.4	2.31	
12	1169.7	3.03	xtl[a]
13	1119.8	4.18	xtl[a]
14	1191.3	2.98	xtl[a]
15	1241.5	2.22	
16	1340.5	1.46	
17	1442.4	0.96	
18	1501.8	0.71	

[a]xtl = subliquidus measurement, some crystals.

Combining the high and low temperature data for remelt experiments, and excluding the data affected by subliquidus crystallization, the best fit Vogel-Fulcher-Tammann (VFT) equation relating melt viscosity (η) and temperature (T) is

$$\log \text{viscosity}\,(\text{Pa s}) = -4.65 + 6653.0/[\text{T(K)} - 531.4] \quad (1)$$

This equation reproduces 26 data points with a root-mean-square error of 0.12 log units.

The four crystallization experiments were conducted after heating to high temperature at 20°C/min, with dwell times of either 0 or 60 min before cooling and measuring viscosity. Very small acicular to skeletal crystals nucleated rapidly, resulting in rapid viscosity increases (Figure 12b). Crystal contents of ~10–60% were estimated from backscattered electron images (Figure 12c) and are reported in Table 4 along with parallel-plate viscosity measurements. As the melt crystallizes, the viscosity increases due to two effects: (i) physical, due to the increase in crystal fraction and (ii) chemical, due to evolving residual liquid composition. We noted considerable variation in the interstitial melt compositions between different experiments, indicative of disequilibrium crystallization, as is expected in this kind of experiment; the range of interstitial melts remained basaltic, however, and did not approach the trachyandesitic glass composition observed in the bombs (Figure 13a). Despite this difference in residual melt composition, both experiments with a 60 min high-temperature dwell produced crystal contents of about 60% and viscosities similar to those of the bulk rock core (Figure 12b). This suggests that the physical effect of crystals is far more important than the small chemical differences between the natural and experimental interstitial melts.

The yield strength experiments all produced qualitatively similar results, with the apparent viscosity of each sample increasing over time (Figure 14). We interpret this to be primarily due to continued crystallization, rather than bubble compaction, because the volume fraction of connected porosity increased in every experiment (Table S2). In all cases the stress-strain rate relationships are notably nonlinear, and concave down, indicating a non-Newtonian shear-thinning rheological behavior. Similar behavior has been noted for basalt [*Ishibashi*, 2009], trachyte [*Vona et al*., 2013], and dacites [*Lavallée et al*., 2007; *Avard and Whittington*, 2012]. The critical question is whether these curves would extrapolate through the origin, or above it, in which case the magmas would exhibit an apparent yield strength. This is most easily estimated by extrapolating the first data from each experiment, when strain rates are highest, especially during the first increasing stress cycle. Linear extrapolation, which places only a maximum constraint on the yield strength, gives intercepts of 30 kPa for a1cL, 20 kPa for a1cR, and 12 kPa for b (Figure 14). Because these are maximum estimates, there is no particular significance that our maximum value for a1cL is greater than for a1cR, which in turn is greater than for b. In brief, while we cannot rule out the existence of a yield strength, we can confidently constrain its magnitude to be relatively small, probably less than 10 kPa.

3.6. Geophysical Results

Following *Ripepe et al*. [2001, 2002], the ascent velocities obtained from the thermal camera data, when integrated with the seismic and acoustic data, should allow us to derive a depth and velocity model for the shallow conduit. Such a model is reported in Figure 6c. Within this model, the depth to the magma free surface (h_c) can be obtained from the delay time between infrasonic and thermal onset (Δt_{i_e}) in

$$h_c = \frac{\Delta t_{i\_e} - x/c}{(U_{\text{jet}} - c')/(c' U_{\text{jet}})} \quad (2)$$

where x is the distance between the vent and the sensor, c is the speed of sound in the atmosphere (340 m s^{-1}), U_{jet} is the speed of the ascending mixture of gas and fragments, and c' is the sound speed in the

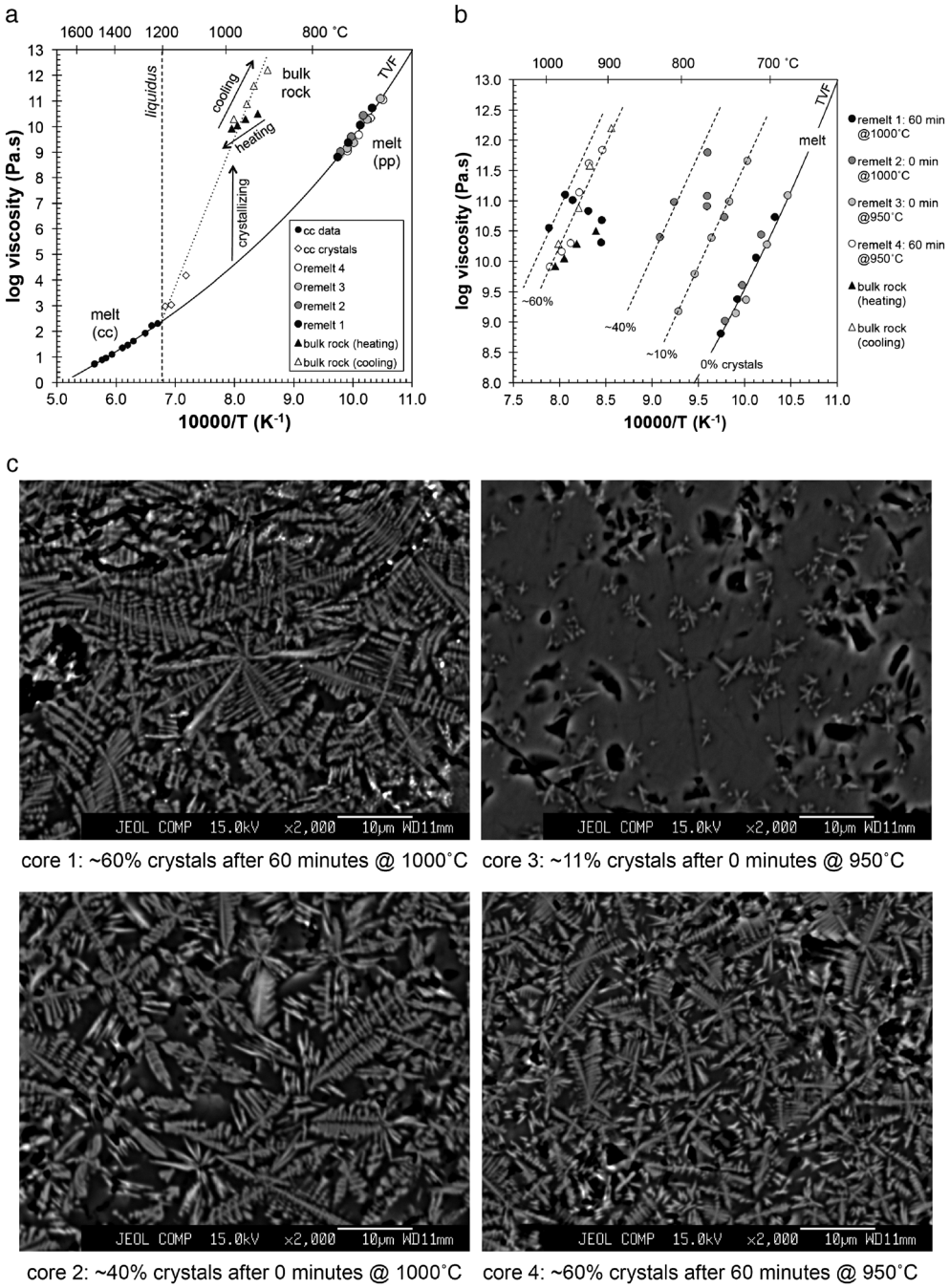

Figure 12. (a) Results of viscosity experiments on cores of a1cL ("bulk rock," triangles) and remelted liquids (circles), plotted as log viscosity versus inverse temperature. Data were collected by parallel-plate (pp) and concentric-cylinder (cc) viscometry and are given in Tables 2 and 3. Open diamonds indicate data for which crystallization affected concentric cylinder measurements. Solid line = best fit VFT equation for melt viscosity. Dashed line = inferred liquidus temperature. Dotted line = extrapolation of concentric cylinder measurements on partially crystallized magma to lower temperatures. (b) Results of crystallization experiments at 950 and 1000°C, with approximate crystal fractions indicated. (c) BSE images showing experimentally produced textures. All scale bars are 10 μm.

conduit (708 m s^{-1}) [*Ripepe et al.*, 2001, 2002]. In this specific case, $\Delta t_{i\ \_\ e}$ is −0.6 s (i.e., the thermal signal is recorded before the infrasonic signal), x is 650 m, and U_{jet} is 48 m s^{-1}. Thus, the resulting distance h_c is 130 m. Given that the hot cloud needs to ascend to a height of 30 m before it can be seen from the ROC site, the conduit length is ~100 m. Now, given the delay time between infrasonic

Table 4. Electron Microprobe Analyses of Interstitial Melts Produced in Crystallization Experiments[a]

	Remelt	Core 3	Core 2	Core 4	Core 1	a1cL
Dwell *T* (°C)		950	1000	950	1000	Matrix
Dwell *t* (min)		0	0	60	60	Glass
% Crystals	0	10	40	60	60	60
	n = 7	*n* = 5	*n* = 2	*n* = 1	*n* = 6	*n* = 10
SiO_2	50.43	51.19	52.27	50.59	51.75	57.62
TiO_2	0.97	1.00	1.00	1.08	0.92	1.43
Al_2O_3	20.18	18.14	18.80	17.11	18.12	16.49
Cr_2O_3	0.01	0.01	0.01	0.01	0.02	0.00
FeO	7.55	7.94	7.92	8.50	8.17	6.70
MnO	0.16	0.17	0.19	0.19	0.19	0.19
MgO	5.10	5.73	5.03	7.08	6.05	3.01
CaO	10.60	11.18	11.07	12.98	11.03	5.57
Na_2O	2.66	2.54	2.56	0.97	3.23	3.40
K_2O	2.32	2.11	1.15	1.49	0.52	5.59

[a]Analyses have been normalized to 100 wt % total.

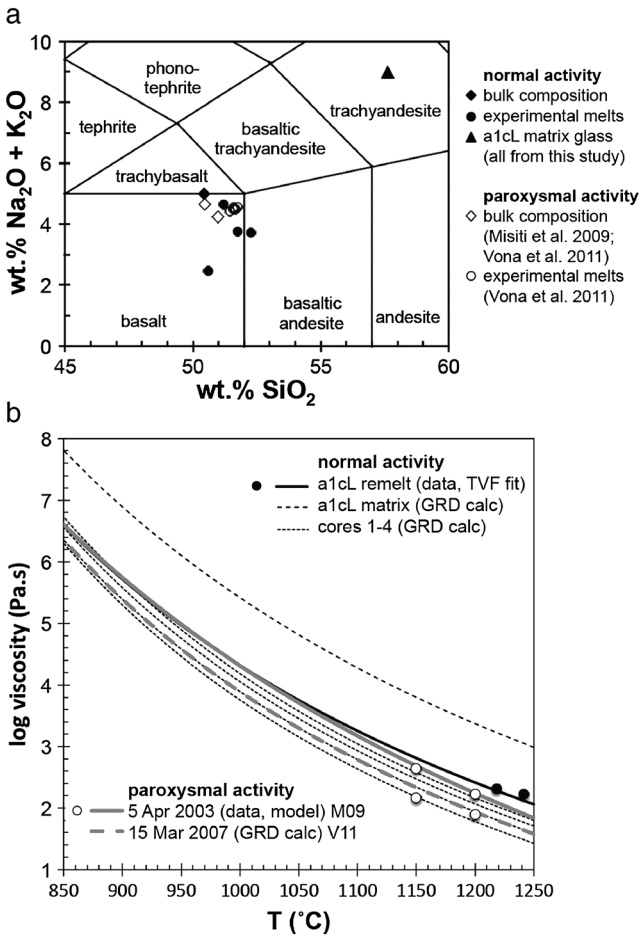

Figure 13. (a) Experimental bulk compositions and experimental residual melt compositions of partially crystalline magmas, plotted on a total alkalis versus silica (TAS) diagram. Closed symbols are from normal activity, open from paroxysmal activity. (b) Comparison of measured and calculated viscosity of melts from normal and paroxysmal eruptions. GRD calc indicates viscosity calculated using the model of *Giordano et al.* [2008]. Compositions for normal activity are a1cL remelt and matrix and experimental cores 1 through 4 (Table 4). Compositions for paroxysmal activity are bulk compositions from *Misiti et al.* [2009] and *Vona et al.* [2013].

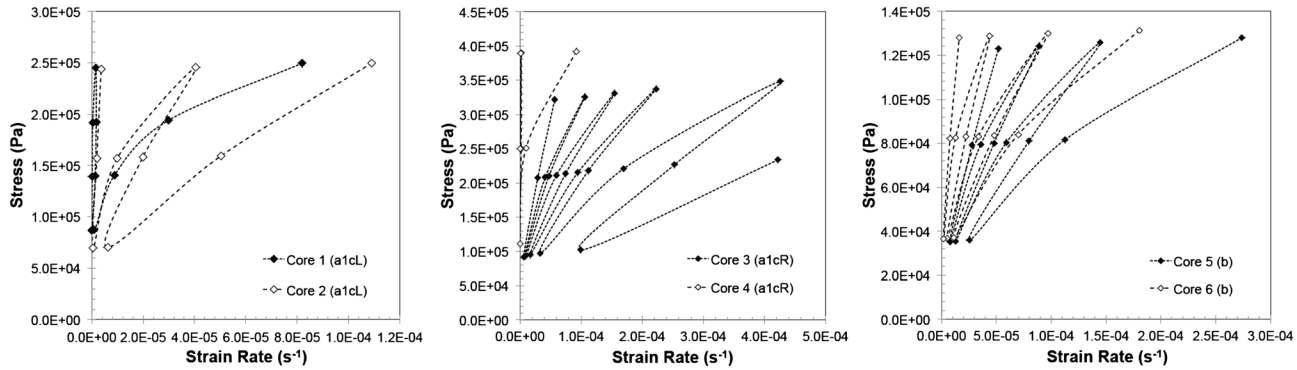

Figure 14. Stress versus strain rate curves for cores of bomb fragments a1cL, a1cR, and b, all collected at ~986°C under uniaxial compression. Dashed lines indicate the order in which points were acquired, always starting with the highest strain rate (lowest apparent viscosity). Full data are given in Table S3.

and seismic onsets, the velocity at which the slug ascends the magma-filled conduit section can be calculated using

$$U = \frac{h - h_c}{\Delta t_{i\_s} - h_c/c^{'} - x/c + r/\alpha} \tag{3}$$

in which U is the slug ascent velocity, h is the depth of VLP signal, Δt_{i_s} is the delay time between infrasonic and seismic onsets, r is the distance between the source and the sensor, and α is the seismic P wave velocity (1600 m s^{-1}) [*Braun and Ripepe*, 1993]. In our case, Δt_{i_s} is 14.4 s (i.e., the VLP is recorded before the explosion), r is 709 m [calculated as $\sqrt{(h^2 + x^2)}$]. Given a typical VLP depth of 290 m for events at the SW crater [*Chouet et al*., 2003; *Marchetti and Ripepe*, 2005], this means that we have a 100 m length of empty conduit and a magma-filled path of 190 m up which the slug rises at a velocity of 13 m s^{-1}. However, the VLP depth for this explosion was deeper, at 450 m, so that the magma-filled path was 350 m long and U was 25 m s^{-1}. Both of these ascent velocities, in agreement with the slug ascent velocities of 10–70 m s^{-1} calculated during normal explosive activity at Stromboli by *Harris and Ripepe* [2007a], are rather high.

4. Discussion

4.1. Textural Facies and Chemical Variations Within the Shallow Magmas at Stromboli

Extraction of textural and chemical features allow us to observe and quantify the fresh (HP magma) and the microlite-rich magma (HPM, HPD, and HPDs magma) that comprise the sampled bombs. All facies coexist side-by-side in the same clast (Figures 2–4). The vesiculated, microlite-free glass resembles the texture and chemistry of the HP scoria described by *Lautze and Houghton* [2005, 2007, 2008], *Polacci et al*. [2006, 2009], and *Colò et al*. [2010]. However, our fresh HP magma lacks the large and deformed vesicles described by the previous authors, who interpreted this as evidence of protracted coalescence and outgassing (Table 5). We observed larger and deformed vesicles only in some HPM facies. The coalescence signature (Figures 8, 9, and S1) is, however, not so a strong as that described by *Lautze and Houghton* [2005, 2007, 2008] in their LD, TT, and HD facies. Interestingly, in the scoriae lapilli that we sampled a few hours later we found strong signature of coalescence, but no evidence of microlites or oxidized olivine [*Colò*, 2012]. Therefore, it seems that the large bombs sample a microlite-rich facies characterized by oxidized olivine. Such a facies has never been described before for Stromboli's shallow magmatic system (Table 5). Micrometer heterogeneities in denser portions of scoriae lapilli have been documented by *Lautze and Houghton* [2005, 2007], but they are microlite poor and chemically homogeneous [*Lautze and Houghton*, 2005]. In contrast, the very dense microlite-rich glass (HPD magma) in our bombs resemble that observed in lava flow and dyke samples from Stromboli [e.g., *Renzulli et al*., 2009], although our HPD facies has a higher proportion of glass. Finally, the HD magma described by *Lautze and Houghton* [2005, 2007, 2008] is poor in small vesicles, while our HPD and HPDs are characterized by a large number of small vesicles in comparison to the HP fresh magma mingled with them. So what is the interpretation of the new facies that we observed and quantified? What is the meaning of the microlites and the oxidized olivine?

AGU Journal of Geophysical Research: Solid Earth 10.1002/2013JB010355

Table 5. Summary of the Textural Features of the HP Magma at Stromboli Known in the Literature

Magma Type and Activity Period	Sample Type	Authors	Density ($\times 10^3$ kg m^{-3})	Glass Color	Vesicles		Crystal Content	Microlite	N_v (mm^{-3})	Glass Matrix Chemistry	Viscosity (Pa s)	Residence Time in the Shallow Conduit	Interpretation
LD 2002	Scoriae lapilli	*Lautze and Houghton* [2005, 2007, 2008]	0.5–0.7	Clear glass	Small-medium-sized vesicles (0.1–3 mm) + big vesicles (3–10 mm) Bimodal trend	Average content (25–50%)	Less abundance of phenocrysts than HD	non	$2–3 \times 10^3$	Typical of HP magma (basaltic-shoshonitic composition	3000 5000	Low residence time (seconds to days)	Slug enclosing material. The little vesicles are due to expansion at fragmentation Increase of LD + MD appears correlated to increase in explosivity
TT 2002	Scoriae lapilli	*Lautze and Houghton* [2007, 2008]	0.7–1.3	Honey glass	Small and big vesicles, but less small vesicles than LD Bimodal trend		In between	non	9×10^2 2×10^3			In between LD and HD	Transitional magma with outgassing and coalescence signatures
MD 2002	Scoriae apilli	*Lautze and Houghton* [2005]	0.7–1.3	Dark + clear	Heterogeneous texture of mingling of LD + HD. The interfaces are marked by big vesicles or phenocrysts		In between	non					Mingled material that appear only within the most energetic explosion
HD 2002	Scoriae lapilli	*Lautze and Houghton* [2005, 2007, 2008]	1.3–1.6	Dark glass	Less small vesicle + amoeboid-like vesicles aligned along the boundary with the LD texture Unimodal trend		More abundance of phenocrysts than LD	non	$2–7 \times 10^2$		2000 2600	Long residence time (days to months)	Outgassed magma, derived from LD left behind by previous explosions that underwent protracted coalescence. The complex big vesicles are considered decoupled from the melt phase and they can contribute to the continuous passive degassing
HP 2003 2004 2005 2006	Scoriae lapilli	*Polacci et al.* [2006, 2008, 2009] *Andronico et al.* [2008]	**Vesicularity** 24–78 35–59		Small spherical vesicles (0.1–0.5 mm), plus large (0.5 – > 4 mm), connected vesicle + a few larger vesicle with channel-like texture Big vesicles can also exhibit foamy, blob-like shapes and composite vesicular shapes	>40%		non	$4–7 \times 10$ 5×10^2 5×10	For the 9/01/09 explosion between HP and LP magma			Magma outgases via interconnected vesicles during protracted vesicle coalescence, while the channel-like texture contributes to the non-explosive degassing. The shallow system is in a steady-state condition
HP 2005 2004 2006	Scoriae lapilli	*Colò et al.* [2010]			Small and large vesicular with a power law Vesicle distribution with exponents ~0.52			non	**Na (mm^{-2})** 10^{-2}				Higher gas content produces more energetic activity, involves more-highly developed magma vesiculation and is associated with high density melt with large vesicles

We are able to exclude the formation of the microlites due to slow posteruption cooling by quenching the bombs as soon as they landed, achieved by pouring water on them. In addition the microlites puncture rounded vesicles of medium and small sizes. Therefore, we interpret the crystallization of microlites to have occurred in the conduit some time after the last vesiculation event that characterized the HPM, the HPD, and the HPDs magmas. The phenocryst-crystallization event is of course the first that happened in the magma chamber, previous to the vesiculation event. The lower vesicularity in the HPD and HPDs facies and their high microlite content (Figure 7) can be explained by more protracted outgassing during longer residence time in the conduit. All of these textural facies represent partly outgassed older magma relative to the HP magma.

The differences in phenocryst and microlite content between each textural facies mean that each facies can be related to portions of magma arriving at different times in the shallow system, to degas, and become stacked up against the conduit wall, as suggested by *Lautze and Houghton* [2005]. They may also remain as a stagnant layer, or an overhang attached to the conduit wall, capping the magma free surface. Some of this cap magma may also represent magma that falls back into the column during fall out from explosive events, as documented at Villarrica by *Gurioli et al*. [2008] during similar activity. We expect that such recycled portions of the mixture will be soft and partially melted, but it is unlikely that they will undergo complete assimilation due to the short time between explosive bursts.

What can the different vesicularity of these magmas tell us? At first glance, the vesicle size distributions seem to be characterized by a single nucleation event and subsequent expansion without a signature of coalescence. However, examination of single textural facies reveals that the HP magma lacks the abundant small vesicles that are apparent in the other three magmas. It also does not have deformed vesicles or strong expansion signatures, as we can observe in, for example, the HPM magma. The HPM magma does, however, have larger vesicles than the HPD and HPDs magmas and they are sometime deformed between the phenocrysts, which formed in the magma chamber before vesicle growth.

Based on these observations, we interpret the HP texture to have formed in fresh (microlite-free) magma that was dispersed or mingled, in very low percentages, with older, recycled, completely (dense parts) or partially (vesiculated zones with microlites) outgassed magmas. The positive correlation between crystallinity and number of small vesicles suggests that the "old" completely or partially outgassed magma was "passively" involved in the vesiculation event of the HP magma, trapping small vesicles, that could have been formed by splitting of larger vesicles [*Belien et al*., 2010]. According to *Belien et al*. [2010], such small bubbles are then enriched in the system (in our case in the HPD and HPDs textural facies) relative to the larger ones because of their slower rise velocity and tendency to stagnate beneath the particles. In contrast, the larger preexisting vesicles further expanded, sometimes becoming deformed because of the abundant phenocrysts of similar dimensions. The variations in glass chemistry observed for both bombs are apparent from an increase in Fe-Ti oxides with increased K (and decreased Fe). The abundant clinopyroxene microlites and microphenocrysts lead to a decrease in Ca in the densest portions (HPD magma), as well as in the vesiculated portions of HPM (Figure 9). As a result, the HPD, HPDs, and HPM glasses plot away from the HP field but on a well-defined linear trend. In Figure 10c we also plot the LP magmas from an air-quenched bomb sampled from a January 2010 explosion at Stromboli [*Gurioli et al*., 2013], which shows a primitive signature.

One further question relates to what triggered the second crystallization event. The population of crystals smaller than 100 μ shows a well-defined crystal habit. The HPM and HPD facies are also characterized by oxidized olivine, rich in magnetite. The process of oxidation occurred subsolidus, after the olivine had already crystallized. This may suggest that the alteration of olivine, as well as the nucleation of mineral phases in the glass matrix such as pyroxene, feldspar, and Ti magnetite, happened during a period of reheating of completely (the HPD and HPDs) or partially degassed magma (HPM), either not ejected or ejected but recycled by previous explosions, that was remelted or kept at high temperature. In this scenario, early degassing of normal HP magma left behind in the shallow system or fallback from previous explosions is followed by air being sucked into the system to create the high fO_2 but still at a temperature above 800°C to allow the crystallization of the magnetite-type minerals [*Haggerty and Baker*, 1967; *Khisina et al*., 1995; *Gualtieri et al*., 2003]. This may indicate that the HPM and HPD magmas were sitting at the magma free surface, above the solidus temperature, under oxidizing conditions. These oxidizing conditions could result from contact with air (as suggested by *Blondes et al*. [2012] for similar texture found in basaltic lava) and/or from sudden decompressions that destabilized a small volume of magma that remains oxidized even after the system is reequilibrated, as suggested by *Cortés et al*. [2006]. In contrast

with *Cortés et al*. [2006], we do not believe that the olivine is from a deeper highly oxidized magma but instead is oxidized at a shallow depth because of reheating or slow cooling of shallow batches of magmas. A similar scenario has been recently proposed by *Del Moro et al*. [2013], to describe oxidation of lithic fragments emitted around the crater area during the 2007 paroxysm events. Here we find similar oxidation characterizing degassed magma in the conduit.

If the HMP, HPD, and HPDs facies truly represent magma residing in the shallow portion of Stromboli's conduit system, what, then, do the lapilli represent? First, we must clarify that for the type 1 [*Patrick et al*., 2007], ballistic-dominated, explosion sampled, bombs are the dominant component in terms of volume and mass [*Gurioli et al*., 2013]. Thus, the opportunity to examine this component allowed us to discover new textural facies that have not, to date, been found in the lapilli-sized scoria samples. Based only on data for the lapilli-sized samples, three different models have been invoked to explain the textural features reported in Table 5. *Lautze and Houghton* [2005, 2007, 2008] proposed a model in which actively vesiculating (low density) melt rises with the gas phase and mingles with more mature (high density) stagnant melt residing in the shallow conduit. In this model, less intense explosions are correlated with an increase in the percentage of the stagnant magma. In addition, *Polacci et al*. [2006, 2008, 2009] interpreted the tortuous-to-channel-like vesicles that they found as preferential pathways for degassing. These form pathways through the fluid magma that can be used by gases that flow nonexplosively to the surface. In contrast, *Colò et al*. [2010] found that the bubble number density (BND) can be correlated with infrasonic activity. Low BND, which reflects a large contribution of big bubbles, correlates with periods of high infrasonic activity, i.e., more vigorous explosions. These results suggest that higher gas contents produce more energetic activity, involve more highly developed magma vesiculation, and are associated with high-density melt with large bubbles. Therefore, if lapilli and bombs all come from the same shallow magma layer in the conduit, why are lapilli microlite free, but bombs are not?

As stated in these previous studies, the lapilli do not contain microlites or oxidized olivine, but they do display coalesced vesicles and gas percolation pathways. Does this texture, characterized by coalesced vesicles, really represent a signature of stagnant magma? A different interpretation was given by *Colò et al*. [2010], who actually correlated the presence of such large vesicles with an increase in the gas flux, not necessarily involving stagnant magma. Because our bombs contain lapilli-like portions, a working hypothesis could be that the bombs consist of both magma that have experienced no, or limited, residence time in the shallow conduit, plus magma of prolonged residence time. This idea is in agreement with both the presence of oxidized olivine crystals, as well as the variable degree of crystallization and chemical evolution of the bombs. But, if this is the case, we now wonder if the coalescence signature is something that happens syneruptively, as proven for relatively more viscous magmas [*Shea et al*., 2012; *Rotella*, 2012] and has nothing to do with the residence time in the conduit as proposed by *Lautze and Houghton* [2007] and Table 5.

4.2. Rheology of Normal Magmas at Stromboli

Two previous studies have measured the viscosity of material erupted during paroxysmal events at Stromboli. *Misiti et al*. [2009] investigated the viscosity of dry and hydrous melts with the bulk composition of the crystal-poor pumice (LP magma) from the paroxysmal eruption on 5 April 2003. Their measurements, using the falling sphere and micropenetration techniques, span a wide range of temperature and water content (450–1400°C and 0.02–4.16 wt % H_2O) for crystal-free melts. *Vona et al*. [2011] investigated the rheology of anhydrous crystal-bearing magmas of similar composition, from the paroxysmal eruption on 15 March 2007, using the concentric cylinder technique between 1187 and 1131°C. Our results, combined with these previous studies, can be used to assess the relative importance of changing chemical composition and crystal content in determining the rheology of Stromboli magmas.

The bulk compositions of the two different magmas, from normal and paroxysmal events (HP and LP, respectively), are remarkably similar (Figure 13a), and it is unsurprising that their remelts show a very similar viscosity (Figure 13b). The variation in viscosity due to changing residual melt composition can be estimated using the model of *Giordano et al*. [2008] to calculate viscosity. For the "normal" magma composition, residual melts from experimental cores 1 through 4 are calculated to have a range of up to 0.5 log units lower than the bulk melt, while the matrix melt from a1cL would be approximately 1 order of magnitude more viscous than the bulk melt (Table S2). For the "paroxysmal" magma composition, residual melts from the experiments of *Vona et al*. [2011] do not vary much from the starting composition (Figure 13a), and their viscosities are

calculated to remain within 0.2 log units of the bulk melt viscosity over the temperature range illustrated in Figure 13b.

In summary, chemical variations in the residual melts of either normal or paroxysmal magmas are likely to contribute no more than a factor of 10 to changes in viscosity from purely molten to at least 60% crystalline. Consequently, rheological variations between melt and magma of many orders of magnitude (Figure 12a) must be primarily attributed to changing crystal content. Bubbles may also play a role, although the similarity in viscosity between experimentally crystallized melt and rock core with several volume percent porosity suggests that crystals have the dominant effect, at least at low-strain rates.

In order to interpret the measured viscosity for the rock core, we calculated matrix liquid viscosity using the *Giordano et al*. [2008] model and the analyzed groundmass composition for a1cL. The predicted viscosity of the interstitial melts is

$$\log \text{viscosity}\,(\text{Pa s}) = -4.55 + 7870.1/(\text{T} - 483.9) \tag{4}$$

$$\log \text{viscosity}\,(\text{Pa s}) = -4.55 + 7726.7/(\text{T} - 498.0) \quad \text{based on our average a1cL} \tag{5}$$

To estimate the viscosity of the mixtures of melt, bubbles, and crystals in the shallow conduit we used the three-phase viscosity treatment of *Phan-Thien and Pham* [1997], as tested on, and applied to, active lavas by *Harris and Allen* [2008]. This treatment gives three cases:

1. Case 1: Crystals smaller than bubbles,

$$\eta(\phi, \phi_{b,}) = \eta_f[1 - v_c/(1 - v_b)]^{-5/2}(1 - v_b)^{-1} \tag{6a}$$

Case 2: Crystals and bubbles are of the same size range,

$$\eta(\phi, \phi_{b,}) = \eta_f(1 - v_c - v_b)^{-(5vc + 2vb)/2(vc + vb)} \tag{6b}$$

Case 3: Crystals larger than bubbles,

$$\eta(\phi, \phi_{b,}) = \eta_f[1 - v_b/(1 - v_c)]^{-1}(1 - v_c)^{-5/2} \tag{6c}$$

in which v_c and v_b are the crystal and bubble volume fractions, respectively, η_f is the fluid viscosity, and $\eta(\phi,\phi_{b,})$ is the three-phase mixture viscosity. We applied the equations depending on the relative size of crystals and bubbles using two end-member situations: (i) a melt temperature of 1200°C, in which case the melt viscosity obtained using equation 1 is 260 Pa s and (ii) a melt temperature of 1000°C, in which case the melt viscosity obtained using equation 4 is 20,860 Pa s. Results are given in Table 6. We see that, at 1200°C, the HP magma has the lowest minimum viscosity of all magmas (850 Pa s). However, in terms of mean viscosity the HPD magma is least viscous (mean = 4600 Pa s), due to its relatively low bubble content (mean = 14%). All other magmas have higher and similar viscosities, mean values being 6600–52 300 Pa s, as result of their higher bubble and crystal contents. Because all of these magmas were well mixed, the viscosity for the "mixture" magma type (6640 Pa s) may be the most appropriate value to describe the viscosity of the shallow system at high temperatures.

If the magma has partly crystallized, this viscosity will be substantially higher, 10^5 Pa s for a mixture at a temperature of 1100°C, and 10^6 Pa s at 1000°C (Table 6). These values are identical to the range (10^5–10^6 Pa s) estimated for lava flows erupted from Stromboli's shallow system during 2003 [*Harris et al*., 2005]. Given that the lava flow is likely just the normal shallow system magma flux escaping from the conduit due to opening of a dyke [*Harris et al*., 2005], this makes sense. In fact, because the lava flows likely represent the immediate escape of magma upon reaching the top of the column, magma normally trapped in the column for some time before release in a Strombolian eruption is probably more likely outgassed and crystalline than that feeding the lava. This explains why some of our densities measured in the two bombs are greater than those obtained for lava flows at Stromboli. Thus, viscosities in the range of $1.2–53.1 \times 10^6$ Pa s for a crystallized, degassed magma mixture in the uppermost portion of Stromboli's conduit seem reasonable.

Table 6. Textural and Rheological Characteristics of Each Magma Type in Stromboli's Shallow Conduit, for the Low (Min), High (Max), and Mean Vesicularity Values From Table 1[a]

	Vesicularity (%)	Crystallinity (%)	Viscosity I ($\times 10^3$ Pa s)	Viscosity II ($\times 10^6$ Pa s)
		Texture: HP		
No.	6			
Min	22	31	0.85	0.86
Max	54	53	19.9	20.2
Mean	36	43	6.6	6.68
SD	13	8	7.5	7.46
		Texture: HPD + HPDs		
No.	7			
Min	1	46	1.95	0.67
Max	25	55	17.4	1.65
Mean	14	50	4.60	1.17
SD	8	4	5.66	0.37
		Texture: HPM		
No.	9			
Min	26	36	1.73	1.76
Max	57	58	180	183
Mean	41	51	52.3	53.1
SD	9	8	73.4	74.9
		Texture: mixture (fresh and outgassed together)		
No.	9			
Min	20	40	3.40	3.46
Max	46	55	9.50	9.66
Mean	33	48	6.64	6.75
SD	8	6	2.10	2.14

[a]We list the fresh magma, HP, the outgassed dense magma (HPD + HPDs), the outgassed vesiculated magma (HPM), and the mixture of all the textural facies Viscosity I is the mixture viscosity calculated for a fluid at 1200°C (260 Pa s) and Viscosity II is the mixture viscosity calculated for a fluid at 1000°C (2.64×10^5 Pa s).

4.3. An Integrated Model for the Shallow Conduit System at Stromboli

The idea of a shallow conduit comprising a mix of vesicular and denser, partly crystallized, and degassed magma has been described for Stromboli by other workers [e.g., *Burton et al.*, 2007; *Lautze and Houghton*, 2005, 2007, 2008; *Polacci et al.*, 2008, 2009; *Colò et al.*, 2010; *Métrich et al.*, 2010; *Bai et al.*, 2011]. In this study we confirm, using straightforward evidence, that outgassed and stagnant magma exists in the shallow portion of the conduit at Stromboli. The presence of fresh and outgassed magma together in the shallow system has important implications for the mechanism that generates explosive events. However, we need to point out that we are looking at bombs erupted during a typical type 1 normal explosion [*Patrick et al.*, 2007] and so can only confidently ascribe our model to such events, or event periods. If we assume that these HPM and HPD magmas degassed and then underwent subsolidus reheating under oxidizing conditions due to contact with the air, the viscosity of the HPM and HPD magmas may be of the order of 10^4–10^5 Pa s, whereas that of the fresh, unoxidized HP magma may be of the order of 10^3 Pa s (Table 6). This means that the magma at the top of the column is a mixture of degassed, oxidized, crystallized, high-viscosity magma and fresh, hot, microlite-poor, low-viscosity magma. It is possible that the high-viscosity magma could even form a rheologically defined layer (still very hot, above 800°C) at the top of the column, through which the fresh magma carried upward by the slug must burst. This may help explain the rather fast propagation velocity of the fragmentation source between the point of VLP generation and the explosion source, i.e., the surface of the magma column in the conduit. If we assume that the slug fills the conduit, then the slug ascent velocity should be proportional to 0.48 $(R_g)^{1/2}$, where R_g is the radius of the conduit [*Batchelor*, 1967]. For a rigid conduit with a radius (R_g) in the range of 1 to 5 m [*Vergniolle and Brandeis*, 1996; *Vergniolle et al.*, 1996], slug velocity should range between 1.5 and 3.4 m/s [*Seyfried and Freundt*, 2000]. This is 1 order of magnitude lower than the velocities obtained from equation 3, i.e., 13–25 m/s. It is difficult to justify this geophysically derived high result and the model on which it is based—that is, that the delay time between the VLP (i.e., slug generation) and infrasonic (i.e., slug bursting) signals is related to simple ascent of a slug between the VLP depth and the explosion level. It seems, instead, we are measuring the velocity at which failure of a highly viscoelastic plug propagates upward from the depth of the VLP to the top of the plug.

This idea has been quantified in this paper but was qualitatively proposed by *Barberi et al.* [1993], who wrote that "the upper part of the Stromboli conduit is filled with a dense, degassed, viscous magma … … … It

would represent an obstacle to the rising gas bubbles, which would accumulate under the degassed, viscous layer up to the time overpressure required for the Strombolian blast is reached". If the outgassed and highly viscous magma forms a plug at the top of the conduit, then why does not this dense material simply plunge back down the conduit? It is possible that successive bursts of explosive activity take place too frequently for convection to be developed in the shallower portion of the conduit, or that an overhang of viscous, sticky material grows outward from the conduit wall to create a dense cap across some of the magma head. This cap sits on top of the actively convecting region, which brings fresh magma up and takes some of the outgassed material down. As such, the cap could potentially provide a plug for persistent degassing too, and possibly it does. *Landi et al*. [2011] propose a model whereby fresher, hotter magma dominates the central conduit and cooler magma the marginal conduits. Indeed, it is the central craters that are characterized by gas puffing, which may dominate the contribution to the total gas flux [*Harris and Ripepe*, 2007a], and the marginal (SW and NE) craters are characterized by explosive activity, from which we have our samples. Gas puffing appears to spread to marginal conduits during phases of higher magma flux [*Landi et al*., 2011]. Indeed, it appears that there are times when the marginal conduits may be free of such cap material, and the degree of capping likely varies with time. The problem is that the dense material can be present at the top of the magma column, and its presence, and temporal/spatial variations in its degree of formation, needs to be taken into account in any dynamic, explosion mechanism, or geophysical model of the conduit.

Given these observations and problems, we thus find it difficult to reconcile our combination of physical and geophysical measurements with a simple model whereby the explosion is explained by ascent of a large slug, in a rheologically uniform and low-viscosity conduit, that bursts cleanly at the magma free surface. Instead, it is possible that on entering the final few hundred meters of the magma-filled conduit, the slug encounters a rheological boundary that then fragments.

5. Conclusions

We define a physical situation, in a Strombolian conduit, whereby we have a population of degassed, oxidized, recrystallized, evolved, and highly viscous magma at the top of the conduit. The fresh, microlite-poor, vesiculated batch responds to the explosive event, apparently by undergoing rapid decompression. Our best model is that the degassed magma forms a plug, or rheologically defined layer, at the top of the conduit, through which the fresh magma bursts. In the light of our data, we need to modify the popular model whereby simple, unimpeded, slug ascent, and free-surface bursting explains the explosive emission. Such a modification is required not only to square with the physical situation defined here for the shallow conduit magma at Stromboli but also to properly explain the sequence of geophysical signals which, when applied to the current model, yield unrealistic results.

Our results also show the importance of sampling the bombs, as well as scoria and ash, during Strombolian events, in parallel with key geophysical and remote sensing measurements. Such a truly multidisciplinary sampling strategy is essential if we are to properly understand, model, and explain the dynamics and mechanisms of Strombolian eruptions, as well as to correctly apply models and assumptions to extract shallow system dynamics from geophysical data sets. In effect, for events such as these, the bombs sample the uppermost section of magma in the conduit, revealing the physical state of the magma just prior to fragmentation and at the point of generation of most of the commonly acquired geophysical metrics for an explosive event. Our results show a rather complex mixture of high- and low-viscosity magmas. Such information is imperative if remotely sensed models and theories are to be deemed valid.

Acknowledgments
We thank J. Siton for the wonderful thin sections that she carefully prepared at University of Hawaii at Manoa (UH). E. Ellebrand and J. Devidal performed the chemistry analyses at UH and Laboratoire Magma et Volcans, respectively. We thank L. Pioli for precious advice and suggestions during the data processing phase. D. Swanson, D. Andronico, and an anonymous reviewer need to be acknowledged for their thoughtful and constructive comments which greatly improved the delivery of our work; their positive and supportive discussions are always appreciated. Field work by A. Harris and analyses at UH were supported by U.S. National Science Foundation grant EAR07-38106. This is Clervolc contribution number 83.

References

Allard, P., J. Carbonnelle, N. Métrich, H. Loyer, and P. Zettwoog (1994), Sulphur output and magma degassing budget of Stromboli volcano, *Nature*, *368*, 326–330.

Andronico, D., and M. Pistolesi (2010), The November 2009 paroxysmal explosions at Stromboli, *J. Volcanol. Geotherm. Res.*, *196*(1-2), 120–125, doi:10.1016/j.jvolgeores.2010.06.005.

Andronico, D., R. A. Corsaro, A. Cristaldi, and M. Polacci (2008), Characterizing high energy explosive eruptions at Stromboli volcano using multidisciplinary data: An example from the 9 January 2005 explosion, *J. Volcanol. Geotherm. Res.*, *176*, 541–550, doi:10.1016/j.jvolgeores.2008.05.011.

Andronico, D., J. Taddeucci, A. Cristaldi, M. Miraglia, P. G. Scarlato, and M. Gaeta (2013), The 15 March 2007 paroxysm of Stromboli: Video-image analysis, and textural and compositional features of the erupted deposit, *Bull. Volcanol.*, *75*, 733, doi:10.1007/s00445-013-0733-2.

Avard, G., and A. G. Whittington (2012), Rheology of arc dacite lavas: Experimental determination at low strain rates, *Bull. Volcanol.*, *74*, 1039–1056, doi:10.1007/s00445-012-0584-2.

Bai, L., D. R. Baker, M. Polacci, and R. J. Hill (2011), In-situ degassing study on crystal-bearing Stromboli basaltic magmas: Implications for Stromboli explosions, *Geophys. Res. Lett.*, *38*, L17309, doi:10.1029/2011GL048540.

Barberi, F., M. Rosi, and A. Sodi (1993), Volcanic hazard assessment at Stromboli based on review of historical data, *Acta Vulcanol.*, *3*, 173–187.

Batchelor, G. K. (1967), *Introduction to Fluid Dynamics*, 615 pp., Cambridge Univ. Press, New York.

Belien, I. B., K. V. Cashman, and A. W. Rempel (2010), Gas accumulation in particle-rich suspensions and implications for bubble population in crystal-rich magma, *Earth Planet. Sci. Lett.*, *297*, 133–140.

Bertagnini, A., N. Métrich, P. Landi, and M. Rosi (2003), Stromboli volcano (Aeolian Archipelago, Italy): An open window on the deep-feeding system of a steady state basaltic volcano, *J. Geophys. Res.*, *108*(B7), 2336, doi:10.1029/2002JB002146.

Blackburn, E. A., L. Wilson, and R. S. J. Sparks (1976), Mechanisms and dynamics of Strombolian activity, *J. Geol. Soc. London*, *132*, 429–440.

Blondes, M. S., M. T. Brandon, P. W. Reiners, F. Zeb Page, and N. T. Kita (2012), Generation of forsteritic olivine (Fo99·8) by subsolidus oxidation in basaltic Flows, *J. Petrol.*, *53*(3), 971–984.

Braun, T., and M. Ripepe (1993), Interaction of seismic and air waves recorded at Stromboli Volcano, *Geophys. Res. Lett.*, *20*, 65–68, doi:10.1029/92GL02543.

Burton, M. R., H. M. Mader, and M. Polacci (2007), The role of gas percolation in quiescent degassing of persistently active basaltic volcanoes, *Earth Planet. Sci. Lett.*, *264*, 46–60, doi:10.1016/j.epsl.2007.08.028.

Chouet, B., N. Hamisevicz, and T. R. McGetchin (1974), Photoballistics of volcanic jet activity at Stromboli, Italy, *J. Geophys. Res.*, *79*, 4961–4976.

Chouet, B., G. Saccarotti, P. Dawson, M. Martini, R. Scarpa, G. De Luca, G. Milana, and M. Cattaneo (1999), Broadband measurements of the source of explosions at Stromboli Volcano, Italy, *Geophys. Res. Lett.*, *26*, 1937–1940.

Chouet, B., P. Dawson, T. Ohminato, M. Martini, G. Saccarotti, F. Giudicepietro, G. De Luca, G. Milana, and R. Scarpa (2003), Source mechanism of explosions at Stromboli Volcano, Italy, determined from moment-tensor inversions of very-long-period data, *J. Geophys. Res.*, *108*(B1), 2019, doi:10.1029/2002JB001919.

Colò, L. (2012), Study of vesiculation in basalt magma through volcanological, textural and geophysical analyses: The case study of Stomboli, PhD dissertation, Department of Earth Sciences, Univ. Firenze, Florence, Italy.

Colò, L., M. Ripepe, D. R. Baker, and M. Polacci (2010), Magma vesiculation and infrasonic activity at Stromboli open conduit volcano, *Earth Planet. Sci. Lett.*, *292*(3–4), 274–280.

Corsaro, R. A., L. Miraglia, and V. Zanon (2005), Petrologic monitoring of glasses in the pyroclastites erupted in February 2004 by the Stromboli Volcano, Aeolian Islands, Southern Italy, *J. Volcanol. Geotherm. Res.*, *139*, 339–443.

Cortés, J. A., M. Wilson, E. Condliffe, and L. Francalanci (2006), The occurrence of forsterite and highly oxidizing conditions in basaltic lavas from Stromboli volcano, Italy, *J. Petrol.*, *47*, 1345–1373.

Del Moro, S., A. Renzulli, P. Landi, S. La Felice, and M. Rosi (2013), Unusual lapilli tuff ejecta erupted at Stromboli during the 15 March 2007 explosion shed light on the nature and thermal state of rocks forming the crater system of the volcano, *J. Volcanol. Geotherm. Res.*, *254*, 37–57.

Delle Donne, D., and M. Ripepe (2012), High-frame rate thermal imagery of Strombolian explosions: Implications for explosive and infrasonic source dynamics, *J. Geophys. Res.*, *117*, B09206, doi:10.1029/2011JB008987.

D'Oriano, C., A. Bertagnini, and M. Pompilio (2011), Ash erupted during normal activity at Stromboli (Aeolian Islands, Italy) raises questions on how the feeding system works, *Bull. Volcanol.*, *73*(5), 471–477.

Francalanci, L., G. R. Davies, W. Lustenmhower, S. Tommasini, P. R. D. Mason, and S. Conticelli (2005), Old crystal re-cycle and multiple magma reservoirs in the plumbing system of the present day activity at Stromboli volcano, South Italy: Sr-isotope in situ microanalyses, *J. Petrol.*, *46*, 1997–2021.

Getson, J. M., and A. G. Whittington (2007), Liquid and magma viscosity in the anorthite-forsterite-diopside-quartz system and implications for the viscosity-temperature paths of cooling magmas, *J. Geophys. Res.*, *122*, B10203, doi:10.1029/2006JB004812.

Giordano, D., J. K. Russel, and D. B. Dingwell (2008), Viscosity of magmatic liquids: A model, *Earth Planet. Sci. Lett.*, *271*(1-4), 123–134.

Gualtieri, A. F., M. Gemmi, and M. Dapiaggi (2003), Phase transformations and reaction kinetics during the temperature induced oxidation of natural olivine, *Am. Mineral.*, *88*, 1560–1574.

Gurioli, L., A. J. L. Harris, B. F. Houghton, M. Polacci, and M. Ripepe (2008), Textural and geophysical characterization of explosive basaltic activity at Villarrica volcano, *J. Geophys. Res.*, *113*, B08206, doi:10.1029/2007JB005328.

Gurioli, L., A. J. L. Harris, L. Colò, J. Bernard, M. Favalli, M. Ripepe, and D. Andronico (2013), Classification, landing distribution and associated flight parameters for a bomb field emplaced during a single major explosion at Stromboli, Italy, *Geology*, *41*, 559–562, doi:10.1130/G33967.1.

Haggerty, S. E., and I. Baker (1967), The alteration of olivine in basaltic and associated lavas. Part I: High temperature alteration, *Contrib. Mineral. Petrol.*, *16*, 233–257.

Harris, A. J. L., and J. S. Allen (2008), One-, two- and three-phase viscosity treatments for Basaltic Lava flows, *J. Geophys. Res.*, *113*, B09212, doi:10.1029/2007JB005035.

Harris, A. J. L., and M. Ripepe (2007a), Synergy of multiple geophysical approaches to unravel explosive eruption conduit and source dynamics—A case study from Stromboli, *Chem. Erde*, *67*, 1–35.

Harris, A. J. L., and M. Ripepe (2007b), Temperature and dynamics of degassing at Stromboli, *J. Geophys. Res.*, *112*, B03205, doi:10.1029/2006JB004393.

Harris, A. J. L., and D. Stevenson (1997), Magma budgets and steady-state activity of Vulcano and Stromboli, *Geophys. Res. Lett.*, *24*, 1043–1046.

Harris, A. J. L., J. Dehn, M. Patrick, S. Calvari, M. Ripepe, and L. Lodato (2005), Lava effusion rates from Hand-Held Thermal Infrared Imagery: An example from the June 2003 effusive activity at Stromboli, *Bull. Volcanol.*, *68*, 107–117.

Harris, A. J. L., M. Ripepe, and E. E. Hughes (2012), Detailed analysis of particle launch velocities, size distributions and gas densities during normal explosions at Stromboli, *J. Volcanol. Geotherm. Res.*, *231-232*, 109–131.

Harris, A. J. L., D. Delle Donne, J. Dehn, M. Ripepe, and K. Worden (2013), Volcanic plume and bomb field masses from thermal infrared camera imagery, *Earth Planet. Sci. Lett.*, *365*, 77–85, doi:10.1016/j.epsl.2013.01.004.

Houghton, B. F., and C. J. N. Wilson (1989), A vesicularity index for pyroclastic deposits, *Bull. Volcanol.*, *51*, 451–462.

Ishibashi, H. (2009), Non-Newtonian behavior of plagioclase-bearing basaltic magma: Subliquidus viscosity measurement of the 1707 basalt of Fuji volcano, Japan, *J. Volcanol. Geotherm. Res.*, *181*, 78–88.

James, M. R., S. J. Lane, B. A. Chouet, and J. S. Gilbert (2004), Pressure changes associated with the ascent and bursting of gas slugs in liquid-filled vertical inclined conduits, *J. Volcanol. Geotherm. Res.*, *129*, 61–82.

Jaupart, C., and S. Vergniolle (1988), Laboratory models of Hawaiian and Strombolian eruptions, *Nature*, *331*, 58–60.

Jaupart, C., and S. Vergniolle (1989), The generation and collapse of a foam layer at the roof of a basaltic magma chamber, *J. Fluid Mech.*, *203*, 347–380.
Khisina, N. R., D. A. Khramov, M. V. Kolosov, A. A. Kleschev, and L. A. Taylor (1995), Formation of ferriolivine and magnesioferrite from Mg–Fe–olivine: Reactions and kinetics of oxidation, *Phys. Chem. Miner.*, *22*, 241–250.
Lacanna, G., and M. Ripepe (2013), Influence of near-source volcano topography on the acoustic wavefield and implication for source modeling, *J. Volcanol. Geotherm. Res.*, *250*, 9–18.
Landi, P., N. Métrich, A. Bertagnini, and M. Rosi (2004), Dynamics of magma mixing and degassing recorded in plagioclase at Stromboli (Aeolian Archipelago, Italy), *Contrib. Mineral. Petrol.*, *147*, 213–237.
Landi, P., E. Marchetti, S. La Felice, M. Ripepe, and M. Rosi (2011), Integrated petrochemical and geophysical data reveals thermal distribution of the feeding conduits at Stromboli volcano, Italy, *Geophys. Res. Lett.*, *38*, L08305, doi:10.1029/2010GL046296.
Lautze, N. C., and B. F. Houghton (2005), Physical mingling of the magma and complex eruption dynamics in the shallow conduit at Stromboli volcano, Italy, *Geology*, *33*, 425–428.
Lautze, N. C., and B. F. Houghton (2007), Linking variable explosion style and magma textures during 2002 at Stromboli volcano, Italy, *Bull. Volcanol.*, *69*, 445–460.
Lautze, N. C., and B. F. Houghton (2008), Single explosions at Stromboli in 2002: Use of clast microtextures to map physical diversity across a fragmentation zone, *J. Volcanol. Geotherm. Res.*, *170*, 262–268.
Lavallée, Y., K. U. Hess, B. Cordonnier, and D. B. Dingwell (2007), Non-Newtonian rheological law for highly crystalline dome lavas, *Geology*, *35*, 843–846.
Marchetti, E., and M. Ripepe (2005), Stability of the seismic source during effusive and explosive activity at Stromboli Volcano, *Geophys. Res. Lett.*, *32*, L03307, doi:10.1029/2004GL021406.
Métrich, N., A. Bertagnini, and A. Di Muro (2010), Conditions of magma storage, degassing and ascent at Stromboli: New insights into the volcano plumbing system with inferences on the eruptive dynamics, *J. Petrol.*, *51*(3), 603–626, doi:10.1093/petrology/egp083.
Misiti, V., F. Vetere, A. Mangiacapra, H. Behrens, A. Cavallo, P. Scarlato, and D. B. Dingwell (2009), Viscosity of high-K basalt from the 5th April 2003 Stromboli paroxysmal explosion, *Chem. Geol.*, *260*(3-4), 278–285.
Ntepe, N., and J. Dorel (1990), Observation of seismic volcanic signals at Stromboli volcano (Italy), *J. Volcanol. Geotherm. Res.*, *43*, 235–251.
Parfitt, E. A. (2004), A discussion of the mechanisms of explosive basaltic eruptions, *J. Volcanol. Geotherm. Res.*, *134*, 131–144.
Parfitt, E. A., and L. Wilson (1995), Explosive volcanic eruptions –IX. The transition between Hawaiian-style lava fountaining and Strombolian explosive activity, *Geophys. J. Int.*, *121*, 226–232.
Patrick, M. R., A. J. L. Harris, M. Ripepe, J. Dehn, D. Rothery, and S. Calvari (2007), Strombolian explosive styles and source conditions: Insights from thermal (FLIR) video, *Bull. Volcanol.*, *69*, 769–784.
Phan-Thien, N., and D. C. Pham (1997), Differential multiphase models for polydispersed suspensions and particulate solids, *J. Non-Newtonian Fluid Mech.*, *72*(2-3), 305–318.
Pistolesi, M., D. Delle Donne, L. Pioli, M. Rosi, and M. Ripepe (2011), The 15 March 2007 explosive crisis at Stromboli volcano, Italy: Assessing physical parameters through a multidisciplinary approach, *J. Geophys. Res.*, *116*, B12206, doi:10.1029/2011JB008527.
Polacci, M., D. R. Baker, L. Mancini, G. Tromba, and F. Zanini (2006), Three-dimensional investigation of volcanic textures by X-ray microtomography and implications for conduit processes, *Geophys. Res. Lett.*, *33*, L13312, doi:10.1029/2006GL026241.
Polacci, M., D. R. Baker, L. Bai, and L. Mancini (2008), Large vesicles record pathways of degassing of basaltic volcanoes, *Bull. Volcanol.*, *70*, 1023–1029.
Polacci, M., D. R. Baker, L. Mancini, S. Favretto, and R. J. Hill (2009), Vesiculation in magmas from Stromboli and implications for normal Strombolian activity and paroxysmal explosions in basaltic systems, *J. Geophys. Res.*, *114*, B01206, doi:10.1029/2008JB005672.
Reed, S. J. B. (1993), *Electron Microprobe Analysis*, Cambridge Univ. Press, Cambridge, U. K.
Renzulli, A., S. Del Moro, M. Menna, P. Landi, and M. Piermattei (2009), Transient processes in Stromboli's shallow basaltic system inferred from dolerite and magmatic breccia blocks erupted during the 5 April 2003 paroxysm, *Bull. Volcanol.*, *71*(7), 795–813.
Ripepe, M., M. Rossi, and G. Saccorotti (1993), Image processing of explosive activity at Stromboli, *J. Volcanol. Geotherm. Res.*, *54*, 335–351.
Ripepe, M., P. Poggi, T. Braun, and E. Gordeev (1996), Infrasonic waves 1005 and volcanic tremor at Stromboli, *Geophys. Res. Lett.*, *23*, 181–184.
Ripepe, M., S. Ciliberto, and M. Della Schiava (2001), Time constraints for modeling source dynamics of volcanic explosions at Stromboli, *J. Geophys. Res.*, *106*, 8713–8727.
Ripepe, M., A. J. L. Harris, and R. Carniel (2002), Thermal seismic and infrasonic evidences of variable degassing rates at Stromboli volcano, *J. Volcanol. Geotherm. Res.*, *118*, 285–297.
Rosi, M., A. Bertagnini, A. J. L. Harris, L. Pioli, M. Pistolesi, and M. Ripepe (2006), A case history of paroxysmal explosion at Stromboli: Timing and dynamics of the April 5, 2003 event, *Earth Planet. Sci. Lett.*, *243*, 594–606.
Rotella, M. D. (2012) Physical processes in subaerial and submarine explosive volcanism: Case studies from the Kermadec Arc, SW Pacific, PhD dissertation, p. 232, School of Geography, Environment and Earth Sciences, Victoria Univ. of Wellington, Wellington, New Zealand.
Scharff, L., M. Hort, A. J. L. Harris, M. Ripepe, J. M. Lees, and R. Seyfried (2008), Eruption dynamics of the SW crater of Stromboli volcano, Italy—An interdisciplinary approach, *J. Volcanol. Geotherm. Res.*, *176*(4), 565–570.
Seyfried, R., and A. Freundt (2000), Experiments on conduit flow and eruption behavior of basaltic volcanic eruptions, *J. Geophys. Res.*, *105*, 23,727–23,740.
Shea, T., B. F. Houghton, L. Gurioli, K. V. Cashman, J. E. Hammer, and B. J. Hobden (2010), Textural studies of vesicles in volcanic rocks: An integrated methodology, *J. Volcanol. Geotherm. Res.*, doi:10.1016/j.jvolgeores.2009.12.
Shea, T., L. Gurioli, and B. F. Houghton (2012), Transitions between fall phases and pyroclastic density currents during the AD 79 eruption at Vesuvius: Building a transient conduit model from the textural and volatile record, *Bull. Volcanol.*, *74*, 2363–2381, doi:10.1007/s00445-012-0668-z.
Slezin, Y. B. (2003), The mechanism of volcanic eruptions (a steady state approach), *J. Volcanol. Geotherm. Res.*, *122*, 7–50.
Taddeucci, J., P. Scarlato, A. Capponi, E. Del Bello, C. Cimarelli, D. M. Palladino, and U. Kueppers (2012), High-speed imaging of Strombolian explosions: The ejection velocity of pyroclasts, *J. Geophys. Res.*, *39*, L02301, doi:10.1029/2011GL050404.
Vanderkluysen, L., A. J. L. Harris, K. Kelfoun, C. Bonadonna, and M. Ripepe (2012), Bombs behaving badly: Unexpected trajectories and cooling of volcanic projectiles, *Bull. Volcanol.*, *74*(8), 1849–1858.
Vergniolle, S., and G. Brandeis (1996), Strombolian explosion: 1. A large bubble breaking at the surface of a lava column as a source of sound, *J. Geophys. Res.*, *101*, 20,433–20,448.
Vergniolle, S., and C. Jaupart (1990), Dynamics of degassing at Kilauea volcano, Hawaii, *J. Geophys. Res.*, *95*, 2793–2809.
Vergniolle, S., G. Brandeis, and J. C. Mareschal (1996), Strombolian explosions. 2. Eruption dynamics determined from acoustic measurements, *J. Geophys. Res.*, *101*, 20,449–20,466.

Vona, A., C. Romano, D. B. Dingwell, and D. Giordano (2011), The rheology of crystal-bearing basaltic magmas from Stromboli and Etna, *Geochim. Cosmochim. Acta*, *75*, 3214–3236.

Vona, A., C. Romano, D. Giordano, and J. K. Russell (2013), The multiphase rheology of magmas from Monte Nuovo (Campi Flegrei, Italy), *Chem. Geol.*, *346*, 213–227.

Whittington, A. G., B. M. Hellwig, H. Behrens, B. Joachim, A. Stechern, and F. Vetere (2009), The viscosity of hydrous dacitic liquids: Implications for the rheology of evolving silicic magmas, *Bull. Volcanol.*, *71*, 185–199.

Wilson, L. (1980), Relationships between pressure, volatile content and ejecta velocity in three types of volcanic explosion, *J. Volcanol. Geotherm. Res.*, *8*, 297–313.

Wilson, L., and J. W. Head (1981), Ascent and eruption of basaltic magma on the Earth and Moon, *J. Geophys. Res.*, *86*, 2971–3001.